International Journal of Non–Linear Mechanics 163 (2024) 104753

Contents lists available at ScienceDirect

International Journal of Non-Linear Mechanics

journal homepage: www.elsevier.com/locate/nlm

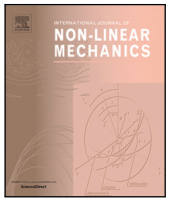

Model reduction to spectral submanifolds in piecewise smooth dynamical systems

Leonardo Bettini, Mattia Cenedese, George Haller *

Institute for Mechanical Systems, ETH Zürich, Leonhardstrasse 21, 8092 Zürich, Switzerland

ARTICLE INFO

Dataset link: https://github.com/haller-group/SSMLearn

Keywords:
Invariant manifolds
Reduced-order modeling
Spectral submanifolds
Piecewise smooth systems

ABSTRACT

We develop a model reduction technique for piecewise smooth dynamical systems using spectral submanifolds. Specifically, we construct low-dimensional, sparse, nonlinear and piecewise smooth models on unions of slow and attracting spectral submanifolds (SSMs) for each smooth subregion of the phase space and then properly match them. We applied this methodology to both equation-driven and data-driven problems, with and without external forcing.

1. Introduction

The ever increasing need to reduce complex, high-dimensional dynamical systems to simple, low-dimensional models has yielded a number of different reduction techniques (see Benner et al. [1], Rowley and Dawson [2], Ghadami and Epureanu [3], Brunton et al. [4], Taira et al. [5] and Touzé et al. [6] for recent reviews). Here, we focus on an extension of one of these methods, spectral submanifold (SSM) reduction, to piecewise smooth mechanical systems.

Defined originally for smooth dynamical systems by Haller and Ponsioen [7], a primary SSM is the smoothest invariant manifold that is tangent to, and has the same dimension as, a spectral subspace of the linearized system at a steady state. As such, SSMs mathematically formalize and extend the original idea of nonlinear normal modes (NNMs) introduced in seminal work by Shaw and Pierre [8,9] and Shaw et al. [10] (see Mikhlin and Avramov [11] for a recent review).

The existence, uniqueness and persistence of SSMs in autonomous and non-autonomous systems have been proven whenever no resonance relationship holds between the linearized spectrum within the spectral subspace and outside that subspace (Haller and Ponsioen [7], Cabré et al. [12] and Haro and de la Llave [13]). The primary SSM tangent to the spectral subspace spanned by the slowest linear modes attracts all nearby trajectories and hence its internal dynamics is an ideal, mathematically justified nonlinear reduced model.

Recent work has revealed the existence of an additional, infinite family of secondary (or fractional) SSMs near the primary one in C^∞ dynamical systems (Haller et al. [14]). Fractional SSMs are also tangent to the same spectral subspace as their primary counterpart, but they are only finitely many times differentiable. Accordingly, they can only be approximated via fractional-powered polynomial expansions.

When the equations of the system are known, its SSMs can be approximated via Taylor expansion at the stationary state using the SSMTool algorithm developed by Jain and Haller [15] and Jain et al. [16]. SSMTool can compute a low-dimensional reduced order model even for systems with hundreds of thousands degrees of freedom. The SSM-reduced models can in turn predict the response of the system to small harmonic forcing (Jain and Haller [15], Jain et al. [17] and Ponsioen et al. [18]) and its bifurcations (Li and Haller [19] and Li et al. [20]). In the absence of governing equations, SSMs and their reduced dynamics can also be approximated from data using the SSMLearn algorithm developed in Cenedese et al. [21]. Such data-driven SSM-reduced models have been found to capture the essentially nonlinear features of autonomous systems and also accurately predict nonlinear response under additional external forcing (Cenedese et al. [21,22,23]). A more recent variant of the same algorithm, fastSSM, provides a simplified, faster SSM-reduction procedure with somewhat reduced accuracy (Axås et al. [24]). Application of these methodologies has proven successful in a variety of examples, both numerical and experimental, ranging from beam oscillations and sloshing in water tank to structural vibrations and transition in shear flows (Cenedese et al. [21,22], Axås et al. [24] and Kaszás et al. [25]).

As most model reduction methods, SSM reduction also assumes that the full system to be reduced is sufficiently many times differentiable. In the absence of the required smoothness, such reduction methods either fail or apply only under modifications. For example,

* Corresponding author.
E-mail address: georgehaller@ethz.ch (G. Haller).

https://doi.org/10.1016/j.ijnonlinmec.2024.104753
Received 15 December 2023; Received in revised form 3 May 2024; Accepted 3 May 2024
Available online 17 May 2024

in Cardin et al. [26,27], the authors showed the existence of a slow manifold in the context of singular perturbation, seeking an extension of invariant manifold-based model reduction for piecewise smooth systems. In particular, they study how the sliding mode present in such systems is affected by singular perturbation and prove that all hyperbolic equilibria and periodic orbits on the sliding region of the reduced problem persist. Motivated by a possible extension of the center manifold reduction of smooth systems to piecewise smooth systems, Weiss et al. [28,29] and Küpper [30] identify invariant cones as tools to reduce the dynamics and study bifurcation phenomena, when the equilibrium lies on the switching manifold between regions of smooth behavior. More precisely, invariant cone-like manifolds are found for nonlinear perturbations of linear piecewise smooth systems and they are constructed starting from a fixed point of the Poincaré map.

A further notable contribution is the study of Szalai [31] on model reduction for non-densely defined piecewise smooth systems in Banach spaces. This highly technical approach uses singular perturbation techniques to develop meaningful reduced order models on low-dimensional invariant manifolds (including SSMs) across switching surfaces. In this paper, we pursue a less technical, but more readily applicable objective. We consider finite-dimensional, piecewise smooth dynamical systems with a single switching surface that contains a fixed point. By extending the two smooth systems from either side of this surface, we conclude the existence of two smooth SSMs, which are separated from each other by a discontinuous jump. We then track full trajectories by appropriately switching between the two SSM-reduced dynamics.

For continuous piecewise linear systems, with no discontinuities across the switching surface, the SSMs would coincide with the slow spectral subspaces. In that setting, Karoui and Leine [32] already put forward the idea of model reduction to two locally invariant half-manifolds. Through the application of a continuous matching approach, those authors remove the discontinuity characterizing the slow manifolds, thereby preserving the continuous nature of the original systems they study.

The structure of this paper is as follows. We first describe our model reduction procedure for piecewise smooth system in Section 2, recalling basic concepts of SSM theory. The normalized non-smoothness parameter is assumed to be small. We then apply this procedure to a simple equation-driven example in Section 3, in which we compute the SSMs analytically and compare several switching strategies among different SSMs. Finally, in Section 4 we discuss a data-driven example of a von Kármán beam for which we carry out model reduction under different types of non-smoothness.

2. Method

For model reduction in a piecewise smooth system, we consider separately the subregions of the phase space in which the system is smooth and apply the results of primary SSM theory separately in those subregions. In particular, we smoothly extend each subsystem locally across its domain boundary and locate primary, smooth SSMs anchored at fixed points in that boundary for the extended system. Such an SSM will only act as an invariant manifold for the full system over its original subregion of smooth dynamics. These various subsets of SSMs form the skeleton of an attractive set for the full system, with pieces of this skeleton connected by trajectories sliding off from them and converging to other pieces of the skeleton (see Fig. 1). The reduced dynamics across different SSM pieces then needs to be connected appropriately by a reduced-order model, as we detail below.

In the following, we first introduce some terminology from the theory of piecewise smooth dynamical systems, then give a more thorough description of our construction of a reduced-order model.

2.1. Piecewise smooth systems

Let us consider the n-dimensional dynamical system

$$\dot{\mathbf{x}} = \mathbf{f}(\mathbf{x};\delta), \quad \mathbf{x}\in\mathbb{R}^n, \quad \delta\in\mathbb{R}, \tag{1}$$

where $\mathbf{x}$ is the state vector and $\mathbf{f}(\mathbf{x};\delta)$ is a nonlinear and piecewise smooth right-hand side, depending smoothly on the parameter δ and the time t, but not necessarily on the phase-space variable $\mathbf{x}$. For simplicity, we assume $\mathbf{f}(\mathbf{x};\delta)$ to be non-smooth across a single hypersurface Σ of dimension $n-1$ that contains the origin $\mathbf{x}=\mathbf{0}$. Namely, the phase space is split into two regions separated by the hypersurface Σ, and $\mathbf{f}(\mathbf{x},\delta)$ is smooth within each of these regions.

The surface Σ is usually called a switching surface, defined by a scalar-valued switching function $\sigma(\mathbf{x})$ as

$$\Sigma = \{\mathbf{x}\in\mathbb{R}^n : \sigma(\mathbf{x}) = 0\} \tag{2}$$

The phase space is then partitioned as $\mathbb{R}^n = \Sigma^+ \cup \Sigma \cup \Sigma^-$, where

$$\begin{aligned} \Sigma^- &= \{\mathbf{x}\in\mathbb{R}^n : \sigma(\mathbf{x}) < 0\}, \\ \Sigma^+ &= \{\mathbf{x}\in\mathbb{R}^n : \sigma(\mathbf{x}) > 0\}. \end{aligned} \tag{3}$$

The original piecewise smooth system (1) can now be written as

$$\dot{\mathbf{x}} = \mathbf{f}(\mathbf{x};\delta) = \begin{cases} \mathbf{f}^+(\mathbf{x};\delta), & \mathbf{x}\in\Sigma^+, \\ \mathbf{f}^-(\mathbf{x};\delta), & \mathbf{x}\in\Sigma^-, \end{cases} \tag{4}$$

where we assume that $\mathbf{f}^\pm(\mathbf{x};\delta)$ both extend to smooth functions of $\mathbf{x}$ in an open neighborhood of Σ. We also assume that

$$\begin{aligned} &\mathbf{f}(\mathbf{x};0) \equiv \mathbf{f}^\pm(\mathbf{x};0), \quad \mathbf{f}(\mathbf{0};0) = \mathbf{0}, \\ &0 \notin \mathrm{Re}[\mathrm{Spect}(\mathrm{D}_{\mathbf{x}}\mathbf{f}(\mathbf{0};0))]. \end{aligned} \tag{5}$$

In other words, for $\delta = 0$, the discontinuity of system (1) disappears and $\mathbf{x}=\mathbf{0}$ is a hyperbolic fixed point of (1), contained in Σ for this value of δ. Note that by the theory developed by Filippov [33], the dynamics within Σ can be approximated by constructing a proper inclusion (see Appendix A.1). According to the convex Filippov's inclusion, the dynamics within the switching surface reads

$$\dot{\mathbf{x}} = \mathbf{f}^\Sigma = \frac{(\mathbf{f}^-\cdot\nabla\sigma)\mathbf{f}^+ - (\mathbf{f}^+\cdot\nabla\sigma)\mathbf{f}^-}{(\mathbf{f}^- - \mathbf{f}^+)\cdot\nabla\sigma}. \tag{6}$$

We assume that trajectories intersecting Σ exhibit two possible behaviors:

- **Crossing**: the orbit crosses through Σ if

$$(\nabla\sigma\cdot\mathbf{f}^+)(\nabla\sigma\cdot\mathbf{f}^-) > 0 \text{ on } \Sigma. \tag{7}$$

- **Sliding**: the orbit slides along the switching surface if

$$(\nabla\sigma\cdot\mathbf{f}^+)(\nabla\sigma\cdot\mathbf{f}^-) < 0 \text{ on } \Sigma. \tag{8}$$

  In the case of sliding, the vector field is tangent to the switching surface and can be expressed as a convex combination of $\mathbf{f}^+$ and $\mathbf{f}^-$ along Σ. The switching surface Σ then either attracts or repels neighboring trajectories, depending on the direction of the vector fields in Σ^+ and Σ^-, as seen in Fig. 2. In the former case, the solution generally evolves along the switching surface. In the latter case, a solution still exists, but it is not unique in forward time.

2.2. Model reduction strategy

We now outline a procedure which allows us to extend SSM-based model reduction to piecewise smooth systems. Our approach utilizes the primary SSMs constructed over slow modes existing on both sides of Σ by the theory of SSMs for smooth systems reviewed in Appendix A.2.

By our assumptions in Section 2.1, for $\delta = 0$, system (1) has a hyperbolic fixed point at $\mathbf{x}=\mathbf{0}$. Any nonresonant spectral subspace E_0 of the linearized system at $\mathbf{x}=\mathbf{0}$ will then admit a unique, primary SSM, $\mathcal{M}_0$, under the addition to the nonlinear terms of $\mathbf{f}(\mathbf{x};0)$. For small $\delta\neq 0$,

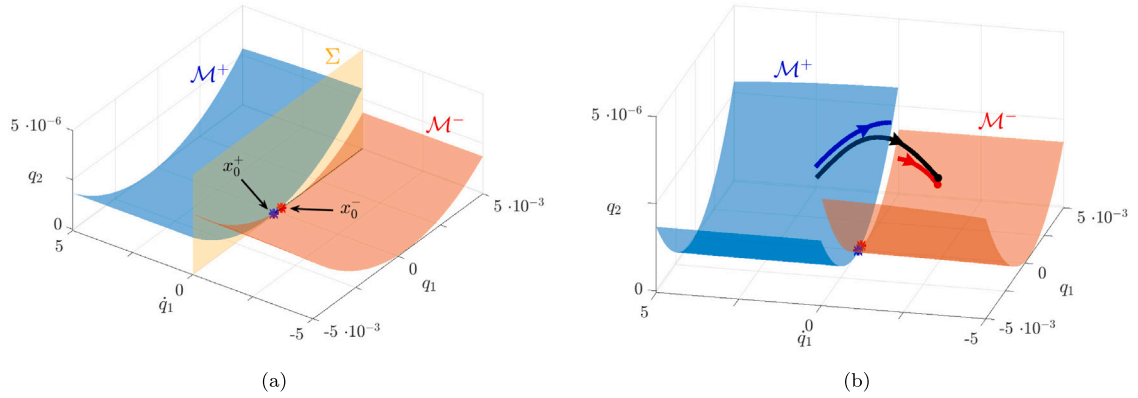

Fig. 1. Reduced-order modeling strategy for piecewise smooth dynamical systems using primary SSMs. The plots depict a specific example, described in Section 4 and reported here for motivation. Fig. (a) represents the two half primary SSMs, $\mathcal{M}^+$ and $\mathcal{M}^-$, anchored at their respective equilibrium points, x_0^+ and x_0^-, and separated by the switching surface Σ. Fig. (b) exemplifies the crossing between two subregions. The black curve is the trajectory of the full system, which is approximated by the reduced dynamics (blue and red curves) lying on $\mathcal{M}^+$ and $\mathcal{M}^-$. The full solution quickly synchronizes with the reduced one, even though the latter involves a physical discontinuity. (For interpretation of the references to color in this figure legend, the reader is referred to the web version of this article.)

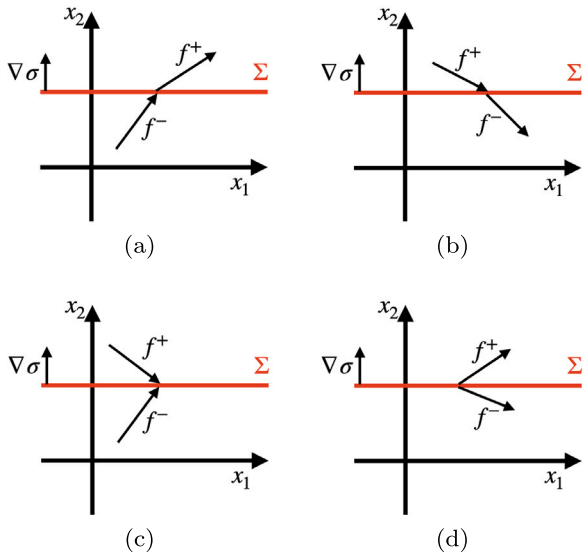

Fig. 2. The orbits can cross either from Σ^- to Σ^+ (a) or from Σ^+ to Σ^- (b). Alternatively, they can exhibit an attracting (c) or a repelling sliding mode (d).

hyperbolic fixed points will continue to exist $\mathcal{O}(\delta)$-close to $\mathbf{x}=\mathbf{0}$ for the two ODEs $\dot{\mathbf{x}} = \mathbf{f}^{\pm}(\mathbf{x};\delta)$ by the implicit function theorem. These fixed points, $\mathbf{x}_0^{\pm}(\delta)$, will have their own SSMs, $\mathcal{M}_\delta^{\pm}$, that are smooth, $\mathcal{O}(\delta)$ perturbations of $\mathcal{M}_0$ by the smooth dependence of SSMs on parameters (Haller and Ponsioen [7]). Restricting $\mathcal{M}_\delta^{\pm}$ in their relevant domains $\Sigma^{\pm}$ defines the half primary SSMs $\mathcal{M}^{\pm}$, which are open and locally invariant sets under (4). As a consequence, the set $\mathcal{M}^+ \cup \mathcal{M}^-$ is a piecewise smooth attracting set for system (1).

We now recall the reconstruction of a general SSM and its reduced dynamics from the data through which the system is observed (see Cenedese et al. [21] and Axås et al. [24] for more detail). We seek the parametrization of the manifold $\mathcal{M}$ as a graph over its *a priori* unknown tangent space $T\mathcal{M}$, which is the image of the spectral subspace E in the space of observables $\mathbf{y} \in \mathbb{R}^n$, where $\mathbf{y}$ collects the variables through which the system is observed. In particular, we approximate the manifold via a multi-variate Taylor expansion

$$\mathbf{y}(\boldsymbol{\eta}) = \mathbf{M}\boldsymbol{\eta}^{1:m} = \mathbf{V}\boldsymbol{\eta} + \mathbf{M}_{2:m}\boldsymbol{\eta}^{2:m}, \tag{9}$$

where $\mathbf{M} = [\mathbf{V}, \mathbf{M}_2, \dots, \mathbf{M}_m]$, with $\mathbf{M}_i \in \mathbb{R}^{n\times d_i}$ and d_i refers to the number of d-variate monomials at order i. We refer to $\boldsymbol{\eta} = \mathbf{V}^T\mathbf{y}$ as reduced coordinates, where the columns of the matrix $\mathbf{V} \in \mathbb{R}^{n\times d}$ are orthonormal vectors that span $T\mathcal{M}$. The notation $(\cdot)^{l:r}$ refers to the vector containing all monomials composed of the entries of the vector $(\cdot)$, with monomials ranging from l to r. In Eq. (9), $l = 1$ and $r = m$. For instance, if $\boldsymbol{\xi} = [\xi_1\xi_2]^T$, then

$$\boldsymbol{\eta}^{2:3} = [\eta_1^2, \eta_1\eta_2, \eta_2^2, \eta_1^3, \eta_1^2\eta_2, \eta_1\eta_2^2, \eta_2^3]^{\mathrm{T}}.$$

Learning $\mathcal{M}$ from a set of training data $\{\mathbf{y}_j\}$ in the observable space means finding the optimal matrix $\mathbf{M}^*$, such that

$$(\mathbf{V}^*, \mathbf{M}^*) = \arg\min_{\mathbf{V},\mathbf{M}_{2:m}} \sum_j \left\| \mathbf{y}_j - \mathbf{V}\mathbf{V}^T\mathbf{y}_j - \mathbf{M}_{2:m}(\mathbf{V}^T\mathbf{y}_j)^{2:m} \right\|, \tag{10}$$

subject to the constraints

$$\mathbf{V}\mathbf{V}^T = \mathbb{I}, \quad \mathbf{V}\mathbf{M}_{2:m} = \mathbf{0}. \tag{11}$$

The dynamics on the SSM in the reduced coordinates $\boldsymbol{\eta}$ can then be approximated as

$$\dot{\boldsymbol{\eta}} = \mathbf{R}\boldsymbol{\eta}^{1:r}, \tag{12}$$

where the elements of $\mathbf{R} \in \mathbb{R}^{d:d_{1:r}}$ are found by solving the minimization problem

$$\mathbf{R}^* = \arg\min_{\mathbf{R}} \left\| \dot{\boldsymbol{\eta}}_j - \mathbf{R}\boldsymbol{\eta}_j^{1:r} \right\|. \tag{13}$$

In the present work, we assume to know *a priori* the model of the system that generates the data $\mathbf{y}_j$, as well as the linear parts of the parametrization (9) and reduced dynamics (12), as in Cenedese et al. [23]. More specifically, in the piecewise smooth context, we suppose that the governing equations, the domains $\Sigma^{\pm}$, and the switching function $\sigma(\mathbf{x})$ defining Σ are known. The slow SSMs analyzed here are normally hyperbolic and hence smoothly persist under differentiable noise in the input to our methodology (Fenichel and Moser [34]).

With these ingredients, we will use the smoothly extended versions of the right-hand sides $\mathbf{f}^{\pm}(\mathbf{x};\delta)$ to generate training data $\{\mathbf{y}_j^{\pm}\}$ from both ODEs $\dot{\mathbf{x}} = \mathbf{f}^{\pm}(\mathbf{x};\delta)$ in a neighborhood of the switching surface. We then construct the SSMs, $\mathcal{M}_\delta^{\pm}$, separately, but only keep their subsets $\mathcal{M}^{\pm}$ falling in the domains $\Sigma^{\pm}$, respectively. Our reduced-order will then switch between the reduced dynamics of $\mathcal{M}^{\pm}$ based on appropriately reduced switching conditions that we will discuss in our upcoming examples.

In this work, we employ an event-driven integration technique based on the single-step, explicit Runge–Kutta ODE45 solver of MATLAB. The method integrates the dynamical system until the switching surface is detected and checks whether condition (8) is satisfied to determine if crossing or sliding is going to occur.

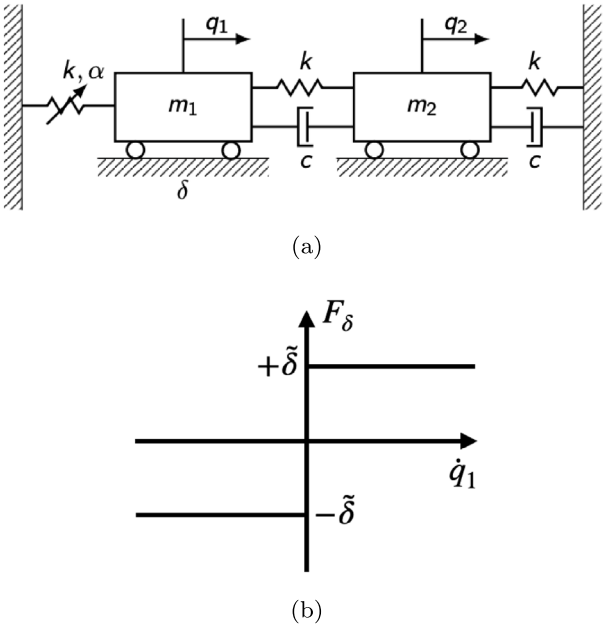

Fig. 3. Two-degree-of-freedom modified Shaw-Pierre mechanical system with friction. (a) System geometry. (b) Coulomb friction law added to the first mass.

3. Example 1: Shaw-Pierre model with friction

We add friction to a modified version of the mechanical system studied by Shaw and Pierre [8], as introduced in Haller and Ponsioen [7]. The resulting system is sketched in Fig. 3.

Dry friction is modeled via the classical Coulomb's law (Leine and Nijmeijer [35]), where the static friction coefficient δ (active when $\dot{q}_1 = 0$) is equal to the dynamic one (valid when $\dot{q}_1 \neq 0$). We now follow the procedure outlined in Section 2 for the computation of a reduced order model for this piecewise smooth system.

Non-smooth formulation. The equations of motion of the system in Fig. 3 are

$$\begin{pmatrix} m_1 & 0 \\ 0 & m_2 \end{pmatrix}\begin{pmatrix} \ddot{q}_1 \\ \ddot{q}_2 \end{pmatrix} + \begin{pmatrix} c & -c \\ -c & 2c \end{pmatrix}\begin{pmatrix} \dot{q}_1 \\ \dot{q}_2 \end{pmatrix} + \begin{pmatrix} 2k & -k \\ -k & 2k \end{pmatrix}\begin{pmatrix} q_1 \\ q_2 \end{pmatrix} + \begin{pmatrix} -\alpha q_1^3 \\ 0 \end{pmatrix} = \begin{pmatrix} -F_\delta(\dot{q}_1) m_1 g \\ 0 \end{pmatrix}, \tag{14}$$

where g denotes the constant of gravity and $F_\delta(\dot{q}_1)$ refers to the friction law in Fig. 3(b), where

$$F_\delta(\dot{q}_1) = \begin{cases} +\tilde{\delta}, & \dot{q}_1 > 0, \\ -\tilde{\delta}, & \dot{q}_1 < 0. \end{cases}$$

In the following, $\delta = \tilde{\delta} g$. With the notation $x_1 = q_1$, $x_2 = \dot{q}_1$, $x_3 = q_2$ and $x_4 = \dot{q}_2$, we can rewrite Eq. (14) as a first-order system of ODEs

$$\dot{\mathbf{x}} = \mathbf{A}_0 \mathbf{x} + \mathbf{f}_{\mathbf{nl}} \mp \mathbf{f}_\delta, \tag{15}$$

with

$$\mathbf{A}_0 = \begin{pmatrix} 0 & 1 & 0 & 0 \\ -\frac{2k}{m_1} & -\frac{c}{m_1} & \frac{k}{m_1} & \frac{c}{m_1} \\ 0 & 0 & 0 & 1 \\ \frac{k}{m_2} & \frac{c}{m_2} & -\frac{2k}{m_2} & -\frac{2c}{m_2} \end{pmatrix},$$

$$\mathbf{f}_{\mathbf{nl}} = \left(0, -\tfrac{\alpha}{m_1} x_1^3, 0, 0\right)^{\mathrm{T}}, \quad \mathbf{f}_{\boldsymbol{\delta}} = \left(0, \delta, 0, 0\right)^{\mathrm{T}}.$$

The sign of the velocity x_2 of the first mass decides whether the friction force is positive or negative, hence this velocity defines the switching function

$$\sigma(\mathbf{x}) = x_2 = \dot{q}_1. \tag{16}$$

Therefore, we have the splitting $\mathbb{R}^4 = \Sigma^+ \cup \Sigma \cup \Sigma^-$, where

$$\Sigma^\pm = \left\{ \mathbf{x} \in \mathbb{R}^4 \,:\, \operatorname{sign}(\sigma(\mathbf{x})) = \pm 1 \right\}. \tag{17}$$

The piecewise smooth system (1) is here specifically defined as

$$\dot{\mathbf{x}} = \mathbf{f}^\pm(\mathbf{x}; \delta) = \begin{pmatrix} x_2 \\ -\frac{2k}{m_1} x_1 - \frac{c}{m_1} x_2 + \frac{k}{m_1} x_3 + \frac{c}{m_1} x_4 - \frac{\alpha}{m_1} x_1^3 \mp \delta \\ x_4 \\ \frac{k}{m_2} x_1 + \frac{c}{m_2} x_2 - \frac{2k}{m_2} x_3 - \frac{2c}{m_2} x_4 \end{pmatrix}. \tag{18}$$

Given that $\nabla\sigma = (0,1,0,0)^{\mathrm{T}}$, a crossing of Σ at a point $\mathbf{x} \in \Sigma$ takes place if $\nabla\sigma \cdot \mathbf{f}^+$ and $\nabla\sigma \cdot \mathbf{f}^-$ have the same nonzero sign at $\mathbf{x}$, i.e.,

$$\begin{cases} -\frac{2k}{m_1} x_1 + \frac{k}{m_1} x_3 + \frac{c}{m_1} x_4 - \frac{\alpha}{m_1} x_1^3 > \delta, \\ -\frac{2k}{m_1} x_1 + \frac{k}{m_1} x_3 + \frac{c}{m_1} x_4 - \frac{\alpha}{m_1} x_1^3 > -\delta, \end{cases} \quad \text{or} \quad \begin{cases} -\frac{2k}{m_1} x_1 + \frac{k}{m_1} x_3 + \frac{c}{m_1} x_4 - \frac{\alpha}{m_1} x_1^3 < \delta, \\ -\frac{2k}{m_1} x_1 + \frac{k}{m_1} x_3 + \frac{c}{m_1} x_4 - \frac{\alpha}{m_1} x_1^3 < -\delta. \end{cases} \tag{19}$$

Attracting sliding motion along Σ ensues when

$$\left| -\frac{2k}{m_1} x_1 + \frac{k}{m_1} x_3 + \frac{c}{m_1} x_4 - \frac{\alpha}{m_1} x_1^3 \right| < \delta. \tag{20}$$

Inside the switching surface Σ, the first mass is in the state of sticking and the second mass acts as a linear harmonic oscillator, i.e., we have

$$\dot{\mathbf{x}} = \begin{pmatrix} 0 \\ 0 \\ x_4 \\ \frac{k}{m_2} x_1 - \frac{2k}{m_2} x_3 - \frac{2c}{m_2} x_4 \end{pmatrix}, \quad \mathbf{x} \in \Sigma. \tag{21}$$

The conditions for repulsive sliding mode are

$$\begin{cases} -\frac{2k}{m_1} x_1 + \frac{k}{m_1} x_3 + \frac{c}{m_1} x_4 - \frac{\alpha}{m_1} x_1^3 > \delta, \\ -\frac{2k}{m_1} x_1 + \frac{k}{m_1} x_3 + \frac{c}{m_1} x_4 - \frac{\alpha}{m_1} x_1^3 < -\delta, \end{cases} \tag{22}$$

which cannot be satisfied for any $\mathbf{x} \in \Sigma$. As a consequence, the Shaw-Pierre system with friction exhibits either crossing or attracting sliding (or sticking) behavior.

We will simulate the behavior of the system with the parameter values used by Shaw and Pierre [8] and Haller and Ponsioen [7],

$$m_1 = m_2 = 1, \quad c = 0.3, \quad k = 1, \quad \alpha = 0.5,$$

and will consider a range of δ values in our analysis.

Analysis of the linearized system. The two different dynamical systems defined in (18) have their own fixed points and smooth SSMs anchored at them. The fixed points are defined by

$$\mathbf{x}_0^\pm = \begin{pmatrix} q_0^\pm \\ 0 \\ \frac{1}{2} q_0^\pm \\ 0 \end{pmatrix}, \tag{23}$$

$$q_0^\pm = \pm \sqrt[3]{-\delta + \sqrt{\delta^2 + 1}} \mp \sqrt[3]{\delta + \sqrt{\delta^2 + 1}}.$$

We shift coordinates so that the origin in the two cases coincides with $\mathbf{x}_0^{\pm}$, respectively:

$$\boldsymbol{\xi}^{\pm} = \mathbf{x} - \mathbf{x}_0^{\pm} = \begin{pmatrix} q_1 - q_0^{\pm} \\ \dot{q}_1 \\ q_2 - \frac{1}{2} q_0^{\pm} \\ \dot{q}_2 \end{pmatrix}. \tag{24}$$

In these coordinates, system (18) becomes

$$\dot{\boldsymbol{\xi}}^{\pm} = \tilde{\mathbf{A}}_0 \boldsymbol{\xi}^{\pm} + \mathbf{f}_{\mathbf{nl}}^{\mathbf{II}}(\boldsymbol{\xi}^{\pm}) + \mathbf{f}_{\mathbf{nl}}^{\mathbf{III}}(\boldsymbol{\xi}^{\pm}) + \mathbf{f}_0, \tag{25}$$

with

$$\begin{aligned} \tilde{\mathbf{A}}_0 &= \begin{pmatrix} 0 & 1 & 0 & 0 \\ -2 - \frac{3}{2}(q_0^{\pm})^2 & -0.3 & 1 & 0.3 \\ 0 & 0 & 0 & 1 \\ 1 & 0.3 & -2 & -0.6 \end{pmatrix}, \\ \mathbf{f}_{\mathbf{nl}}^{\mathbf{II}}(\boldsymbol{\xi}^{\pm}) &= \left(0, -\frac{3}{2} q_0^{\pm} \left(\xi_1^{\pm}\right)^2, 0, 0\right)^{\mathrm{T}}, \\ \mathbf{f}_{\mathbf{nl}}^{\mathbf{III}}(\boldsymbol{\xi}^{\pm}) &= \left(0, -\frac{1}{2} \left(\xi_1^{\pm}\right)^3, 0, 0\right)^{\mathrm{T}}, \\ \mathbf{f}_0 &= \left(0, -\frac{3}{2} q_0^{\pm} - \frac{1}{2}(q_0^{\pm})^3 \mp \delta, 0, 0\right)^{\mathrm{T}}. \end{aligned} \tag{26}$$

The matrix $\tilde{\mathbf{A}}_0$ is unaffected by the sign choice in $q_0^{\pm}$, therefore both cases have the same spectral properties and hence the same spectral subspaces.

The eigenvalues of $\tilde{\mathbf{A}}_0$ for $\delta = 10^{-1}$ are

$$\begin{aligned} \lambda_{1,2} &= -0.0741 \pm i\, 1.0027, \\ \lambda_{3,4} &= -0.3759 \pm i\, 1.6812, \end{aligned}$$

whose eigenvectors give rise to two two-dimensional real invariant subspaces, E_1 and E_2.

3.1. Computation of SSMs

According to the definition given in Appendix A.2, the relative spectral quotients of E_1 and E_2 are

$$\sigma(E_1) = \mathrm{Int}\left[\frac{\mathrm{Re}\,\lambda_{3,4}}{\mathrm{Re}\,\lambda_{1,2}}\right] = 5. \tag{27}$$

Changing the friction coefficient δ has a mild effect on the eigenvalues and hence the spectral quotients will not change for the range of friction coefficients studied here. Considerations about the existence and uniqueness of the SSMs in the positive and negative cases are exactly the same, as they share the same linearized dynamics, even though they are anchored at different points. The nonlinear contribution of the spring $\mathbf{f}_{\mathbf{nl}}$ is an autonomous term that is analytic on the whole phase space.

Based on these facts, the results in Haller and Ponsioen [7] guarantee the existence and uniqueness of the slow two-dimensional SSM, $\mathcal{M}_1(0)$, because the required nonresonance conditions among the eigenvalues are satisfied up to order $\sigma(E_1)$ (see Haller and Ponsioen [7] for details). Therefore, we can state that the analytic SSM $\mathcal{M}_1(0)$ exists and it is unique among all C^6 invariant manifolds tangent to E_1 at the origin. We introduce coordinates aligned with E_1 and E_2 by letting

$$\boldsymbol{\xi}^{\pm} = \mathbf{V}\boldsymbol{\eta}^{\pm}, \tag{28}$$

where

$$\boldsymbol{\eta}^{\pm} = (\mathbf{y}^{\pm}, \mathbf{z}^{\pm}) \in E_1 \times E_2,$$

and $\mathbf{V}$ is the matrix whose columns are the eigenvectors of $\tilde{\mathbf{A}}_0$. The reduced coordinates $\mathbf{y}^{\pm}$ act as the master variables over which we seek the slow SSM as a graph.

We report the analytical computation of the SSM in Appendix A.3.

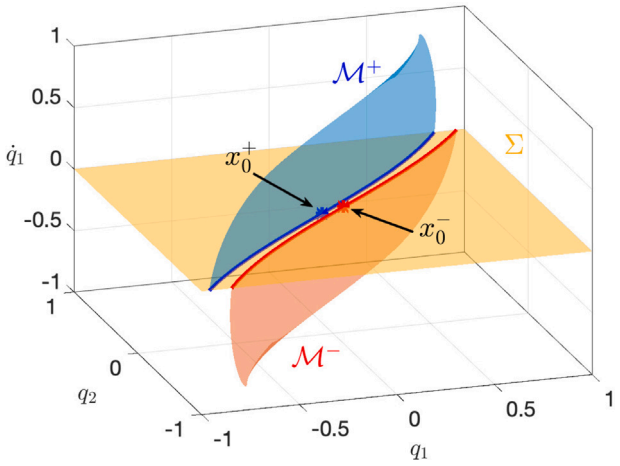

Fig. 4. The two half primary SSMs $\mathcal{M}^+$ and $\mathcal{M}^-$, separated by the switching surface Σ, for $\delta = 10^{-1}$. The blue and the red lines are the intersection of the primary SSMs $\mathcal{M}_\delta^{\pm}$ defined in the whole state space with the switching surface. (For interpretation of the references to color in this figure legend, the reader is referred to the web version of this article.)

3.2. Combination of SSMs and the switching surface

We now restrict the SSMs constructed at $\mathbf{x}_0^{\pm}$ to their region of validity imposed by condition (17). The resulting restricted SSMs are separated by the switching surface Σ, as seen in Fig. 4.

As the two pieces of primary SSMs form an attracting set for the full system, the dynamics restricted to them provides a reduced-order model for nearby initial conditions. We now describe how we connect the dynamics across the different SSM pieces when a trajectory hits the switching surface and satisfies the crossing condition (19). In this scenario, coming from one SSM, we need a new initial condition lying on the other one. By Fig. 5, the intersection between the incoming trajectory and the switching surface (blue dot in Fig. 5(a)) is associated to a set of both reduced $\mathbf{y}^{\pm} = \left(y_1^{\pm}, y_2^{\pm}\right)^{\mathrm{T}}$ and observable $\mathbf{x} = \left(q_1, \dot{q}_1, q_2, \dot{q}_2\right)^{\mathrm{T}}$ coordinates. We then exploit the relationship between the two sets of reduced coordinates for the two SSMs to find the new initial condition (red dot in Fig. 5(a)) as

$$\begin{pmatrix} y_1^- \\ y_2^- \end{pmatrix} = \begin{pmatrix} y_1^+ \\ y_2^+ \end{pmatrix} + \mathbf{V}_{12}^{-1}(\mathbf{x}_0^+ - \mathbf{x}_0^-), \tag{29}$$

where the rectangular matrix $\mathbf{V}_{12}^{-1}$ contains the first two rows of $\mathbf{V}^{-1}$. Formula (29) defines the new initial condition on $\mathcal{M}^-$ as the projection of the final point on $\mathcal{M}^+$ onto $\mathcal{M}^-$. In other words, we are assuming that the fast dynamics dominates the slow dynamics across the switching surface and along a linear approximation of the stable fiber of $\mathcal{M}^-$, to which the blue point belongs. As a result, the new initial condition defines a trajectory on the manifold that approximates the one to which the trajectory of the full dynamics converges the fastest.

Coming from $\mathcal{M}^+$, the new initial condition (y_1^-, y_2^-) on $\mathcal{M}^-$ according to Eq. (29) does not lie in the intersection between the $\mathcal{M}_\delta^-$ and the switching surface (orange line). As a consequence, all physical variables experience a discontinuity while crossing from one SSM to the other. Discontinuities in the solution are unavoidable, but one can investigate further strategies in order to enforce physical consistency for specific variables, as seen in Fig. 5.

Studying the reduced dynamics according to these various choices in a time frame when only crossing occurs, we observe that the initial condition defined by (29) tracks the full solution most accurately (see Appendix A.3.2). Therefore, we will use this matching scheme for initial conditions in the following.

If the sliding condition (8) is satisfied for the reduced dynamics across the switching surface, then sliding occurs instead of crossing.

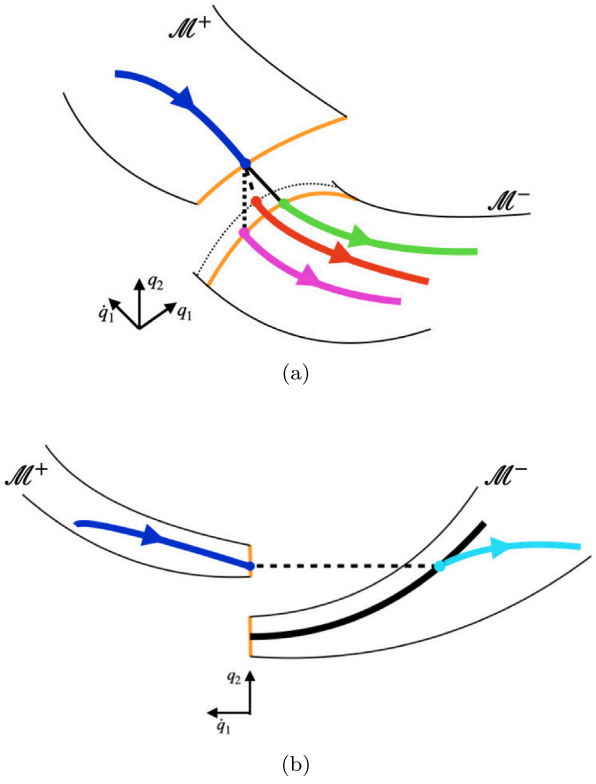

Fig. 5. Different strategies for the computation of the new initial condition of the reduced dynamics across the switching surface Σ. The orange lines represent the intersection of the SSMs with Σ. When a trajectory on one SSM (blue line) hits the switching surface, the projection of the intersection point onto the new SSM according to Eq. (29) (red dot) represents a new initial condition. Alternatively, we can enforce that the new initial condition lies on the switching surface, minimizing the difference of all physical variables across the jump (green dot) or ensuring the continuity of q_1 (purple dot). If we require that both q_1 and q_2 are continuous (light blue dot), then the new initial condition lands far from the switching surface. The black line in (b) depicts the set of points on the manifold $\mathcal{M}^-$ with the same value of q_1 as the final point of the blue trajectory on $\mathcal{M}^+$. (For interpretation of the references to color in this figure legend, the reader is referred to the web version of this article.)

In such a case, the convex Filippov inclusion provides us with a closed form for the dynamics within the switching surface (6), as explained in Section 2.1 and detailed in Appendix A.1. In this context, the $\mathbf{f}^+$ and $\mathbf{f}^-$ present in Eqs. (6) and (8) denote the reduced dynamics on $\mathcal{M}^+$ and $\mathcal{M}^-$.

3.3. Poincaré map and invariant set

We now seek an actual attractor (i.e., a closed invariant set with an open domain of attraction) near the locally invariant, attracting set $\mathcal{M}^+ \cup \mathcal{M}^-$. More specifically, we seek the intersection of this attractor with the switching surface Σ. To this end, we consider a set of initial conditions around the intersection of $\mathcal{M}_\delta^\pm$ with Σ in the $(q_1, q_2, \dot{q}_2)$ space and let them evolve until the sticking regime is reached. Recording the crossing of trajectories through Σ defines a Poincaré map, which reveals an invariant curve Γ with a discontinuity close to the origin (green straight piecewise continuous line in Fig. 6). The two segments of this invariant curve lie in proximity to the intersection of $\mathcal{M}_\delta^\pm$ with Σ (blue and red lines) on either side of the origin. The points at the discontinuity of Γ are denoted as $x_{edge}^\pm$. The preimages of $x_{edge}^\pm$ under the Poincaré map correspond to the intersections of Γ with the surfaces that defines the sticking conditions ($x_{pre}^\pm$ in Fig. 6(a)). In particular, these points define the edge states for which crossing is still possible. In these states, the sum of forces from springs and dampers is almost equal to the static friction force, but sufficient to induce crossing. The invariant curve Γ and $x_{edge}^\pm$ have been computed integrating the full model, but they can be directly approximated from the reduced-order model (see Appendix A.3.3).

3.4. Non-autonomous problem

Under small periodic external force applied to both masses, system (1) becomes

$$\begin{pmatrix} m_1 & 0 \\ 0 & m_2 \end{pmatrix}\begin{pmatrix} \ddot{q}_1 \\ \ddot{q}_2 \end{pmatrix} + \begin{pmatrix} c & -c \\ -c & 2c \end{pmatrix}\begin{pmatrix} \dot{q}_1 \\ \dot{q}_2 \end{pmatrix} + \begin{pmatrix} 2k & -k \\ -k & 2k \end{pmatrix}\begin{pmatrix} q_1 \\ q_2 \end{pmatrix} + \begin{pmatrix} -\alpha q_1^3 \\ 0 \end{pmatrix} \pm \begin{pmatrix} \delta m_1 \\ 0 \end{pmatrix} = \epsilon \frac{1}{\sqrt{2}}\begin{pmatrix} 1 \\ 1 \end{pmatrix} \cos \Omega t, \tag{30}$$

where $0 \leq \epsilon << 1$. In terms of the coordinates introduced in Eq. (24) and the quantities defined in Eq. (26), we have

$$\dot{\boldsymbol{\xi}}^\pm = \tilde{\mathbf{A}}_0 \boldsymbol{\xi}^\pm \pm \mathbf{f}_{\mathbf{nl}}^{\mathbf{II}}(\boldsymbol{\xi}^\pm) + \mathbf{f}_{\mathbf{nl}}^{\mathbf{III}}(\boldsymbol{\xi}^\pm) + \mathbf{f}_0 + \epsilon\, \mathbf{f}_\epsilon(\Omega t), \tag{31}$$

with

$$\mathbf{f}_\epsilon = \frac{1}{\sqrt{2}}\begin{pmatrix} 0 \\ \frac{1}{m_1} \\ 0 \\ \frac{1}{m_2} \end{pmatrix} \cos \Omega t = \mathbf{f}_0 \cos \Omega t.$$

To obtain an approximation for the time-dependent SSMs on the two sides of the switching surface, we again rely on a cubic Taylor expansion, but with the addition of a $2\pi/\Omega$-periodic time-dependent term (the details are reported in Appendix A.3.4).

We now compare the SSM-reduced model with the full-order one in terms of forced response curves computed for different forcing amplitudes $|\mathbf{f}_0|$ and friction coefficients δ. For each case, we compute the response of the full system using the numerical continuation software COCO of Dankowicz and Schilder [36] for a range of forcing frequencies. In contrast, results of the reduced model come from the direct integration of the reduced dynamics.

Fig. 7 shows highly accurate predictions for forced responses for the smallest value of the forcing amplitude ϵ, even for large values of δ. Generally, the prediction error grows for larger forcing amplitudes. This behavior arises from higher amplitude responses, if we maintain the same order of approximation for the SSM (in this case cubic). Indeed, as detailed in Appendix A.3.1, the invariance error grows with the response amplitude.

Consequently, the observed discrepancy between the full- and reduced-order model at high values of ϵ (shown in the subplots 7(a), 7(b) and 7(c)) can be reduced by just increasing the order of approximation of the SSM. In contrast, for larger δ values (see sub Fig. 7(d)), the amplitude response remains low enough for the reduced-order model based on cubic order SSM approximation to be sufficiently accurate, even for higher forcing amplitudes.

4. Data-driven model reduction of a piecewise smooth beam model

We now apply our nonsmooth SSM-reduction procedure in a data-driven setting. We consider a finite-element model of a von Kármán beam with clamped-clamped boundary conditions. Each finite element has three degrees of freedom: axial deformation, transverse displacement and transverse rotation. The beam is approximated by four elements with uniform grid, resulting in a total of 9 degrees of freedom, i.e., in an 18-dimensional phase space. The finite-element discretization is carried out using elements featuring cubic shape functions for the transverse deflection and linear shape functions for the axial displacement (Jain et al. [17]). The material is aluminium, with Young modulus $E = 70\,\text{GPa}$, density $\rho = 2700\,\text{Kg/m}^3$, Poisson ratio $\nu = 0.3$ and material

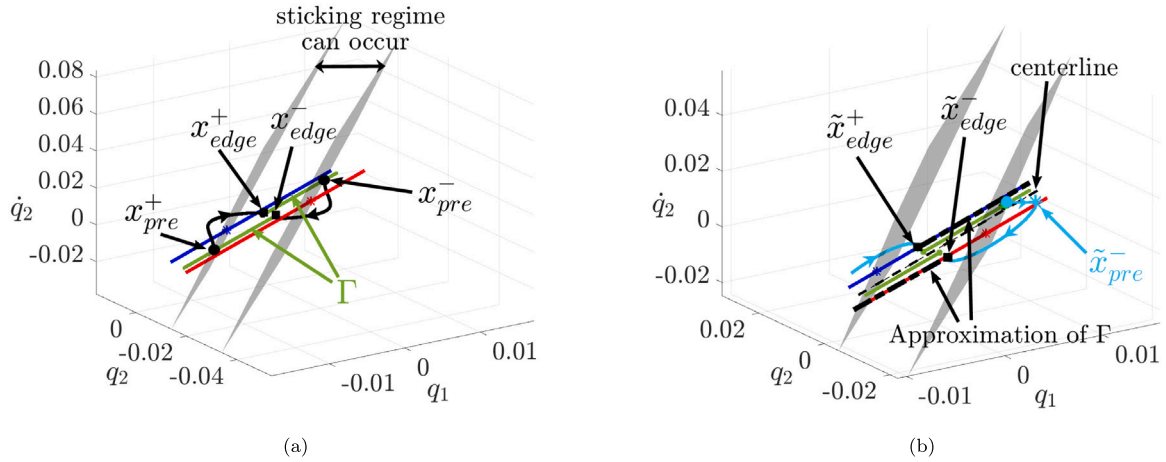

Fig. 6. The invariant curve Γ (in green) of the Poincaré map for the Shaw-Pierre model with friction presents a discontinuity close to the origin. The gray surfaces delimit the region where the sticking regime can occur if $\dot{q}_1 = 0$ and contain the two fixed points $x^{\pm}_0$. (a): $x^{\pm}_{edge}$ are the iterates of the edge configurations for which crossing is possible ($x^{\pm}_{pre}$), before entering the sticking regime, according to the full-order model. (b): an approximation of the invariant curve Γ is derived as a portion of the blue and red lines, namely the intersection of the positive and negative SSMs with the switching surface, where $\tilde{x}^{\pm}_{edge}$ are the iterates of $\tilde{x}^{\pm}_{pre}$. (For interpretation of the references to color in this figure legend, the reader is referred to the web version of this article.)

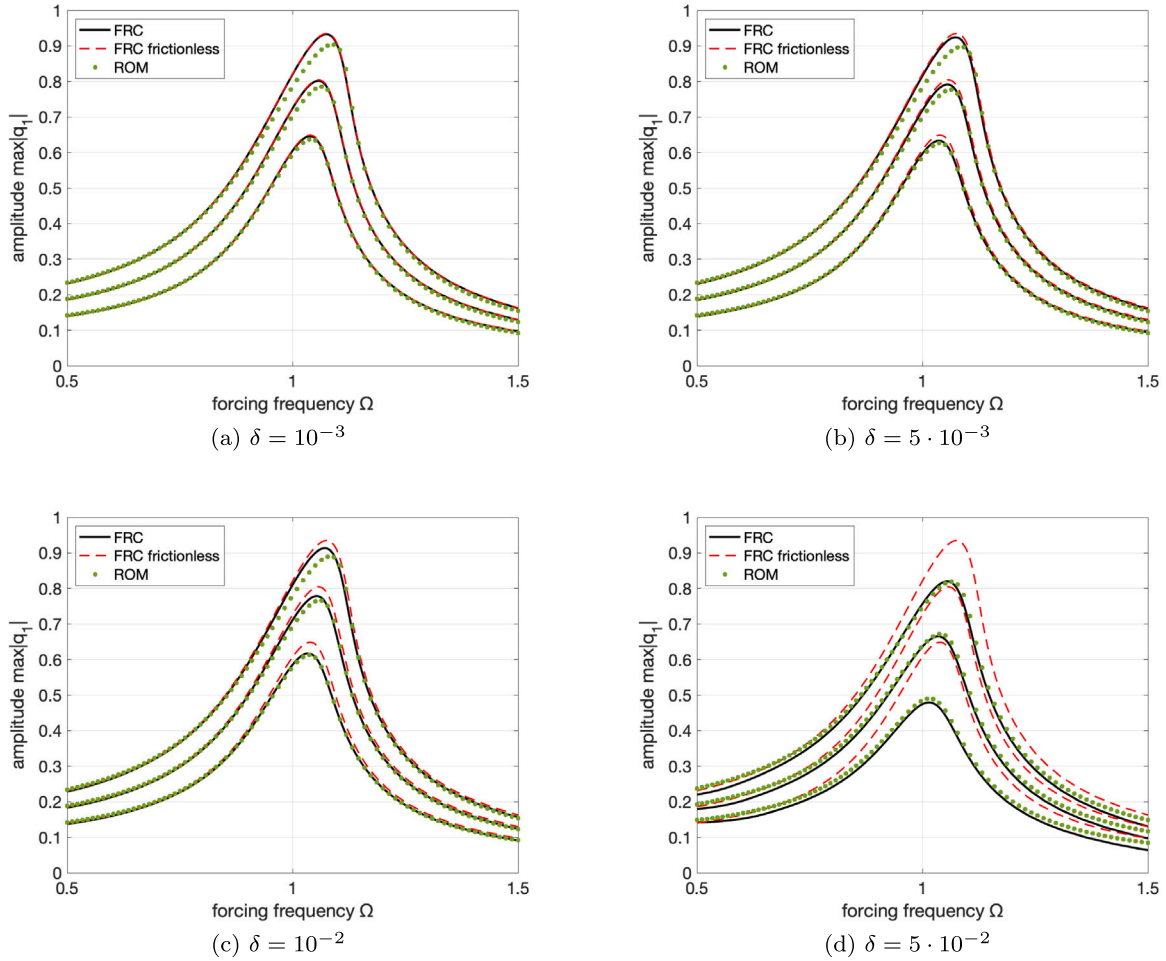

Fig. 7. Forced response curves for the forced Shaw-Pierre example with friction, obtained for different values of the friction coefficient δ. For each case, the amplitudes of the forcing (ϵ in Eq. (30)) are 0.15, 0.2 and 0.25. The black curves represent the solution of the full-order model; the red dashed curves indicate the forced response without friction; the set of green dots represents the reduced-order model approximation.

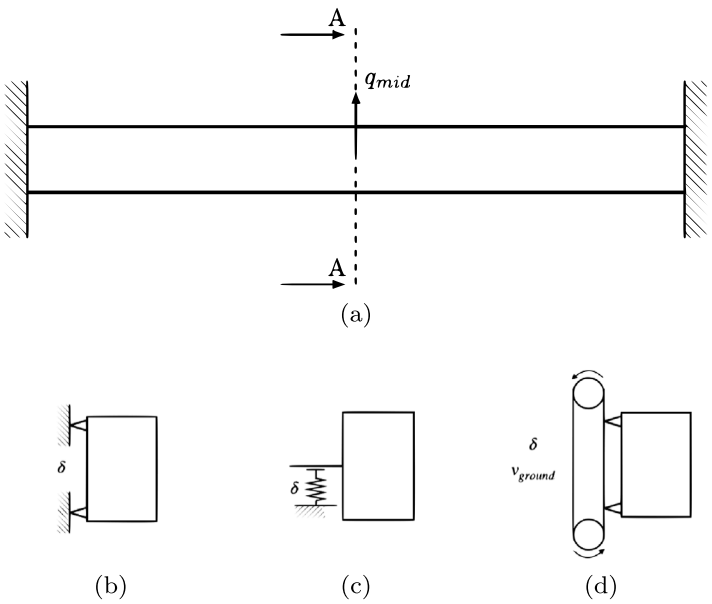

Fig. 8. (a) Geometry of the clamped-clamped von Kármán beam. In each of the cases shown in the subplots (b), (c), (d), the non-smoothness is localized at the midpoint section A-A, where q_{mid} represents the vertical displacement of the beam in that section. (b): Coulomb friction, (c) soft impact, (d) friction on moving ground.

damping modulus $k = 1 \times 10^6$ Pa s. We set the length 1 [m], the width 5 [cm] and the thickness 2 [cm].

We consider three different cases of non-smoothness introduced at the middle of the beam (section A-A of Fig. 8(a)), with the parameter δ playing a different role in each case.

1. **Coulomb friction:** Dry friction is present in the vertical motion of the beam, in its middle section, as seen in Fig. 8(b). The resulting switching function reads

$$\sigma(\mathbf{x}) = \dot{q}_{mid}, \tag{32}$$

and the switching surface

$$\Sigma^{\pm} = \left\{\mathbf{x} \in \mathbb{R}^N \,:\, \text{sign}(\sigma(\mathbf{x})) = \pm 1\right\}, \tag{33}$$

with N denoting the phase space dimension of the discretized beam model. Once discretization has been performed, the equations read

$$M\ddot{\mathbf{q}} + C\dot{\mathbf{q}} + K\mathbf{q} + \mathbf{f}_{nl}(\mathbf{q}, \dot{\mathbf{q}}) = \mathbf{f}_{\delta}^{\pm}, \tag{34}$$

where

$$\mathbf{f}_{\delta}^{\pm} = (0 \cdots 0, \mp\delta, 0 \cdots 0)^T. \tag{35}$$

In Eq. (35), the forcing acts only on the element located at the midpoint. The behavior within the switching surface is qualitatively the same as in the Shaw-Pierre example of Section 3, in that both crossing and attractive sliding (sticking) regimes are possible. We define a normalized non-smooth coefficient $\tilde{\delta}$ by dividing δ by the maximal elastic force at the midpoint.

2. **Soft impact:** The section A-A of the beam collides with a spring when the vertical displacement is negative. The switching function now is

$$\sigma(\mathbf{x}) = q_{mid}. \tag{36}$$

Formally, Eq. (34) is still valid, but

$$\mathbf{f}_{\delta}^{+} = \mathbf{0}, \quad \text{and} \quad \mathbf{f}_{\delta}^{-} = (0 \cdots 0, -\delta x_{mid}, 0 \cdots 0)^T. \tag{37}$$

The behavior of the system is asymmetric with respect to the $q_{mid} = 0$ position, due to the presence of the further stiffness on one side, as seen in Fig. 9.

According to conditions (7) and (8), only crossing between the regions Σ^+ and Σ^- is admissible, while sticking is not allowed. In this case, the coefficient δ represents the increased stiffness acting on the midpoint of the beam for $q_{mid} < 0$ and it is naturally normalized by the linear stiffness of the beam.

3. **Friction on moving ground:** Assume that the midpoint of the beam rides on a belt moving with constant velocity v_{ground} (Fig. 8(d)) and dry friction is present between the beam and the belt. The piecewise smooth forcing term is then given by

$$\mathbf{f}_{\delta}^{\pm} = (0 \cdots 0, \delta f_{ns}, 0 \cdots 0)^{\mathrm{T}}, \tag{38}$$

where

$$f_{ns}(\dot{q}_{mid}) = -\text{sign}\,(\dot{q}_1 - v_{ground}) \times \left(1 + \frac{\alpha}{e}\exp\left(\frac{\beta - |\dot{q}_{mid} - v_{ground}|}{\beta}\right)\right), \tag{39}$$

as shown in Fig. 10. This friction model, similar to that used in Leine and Nijmeijer [35], takes into account that the value of the static friction to be overpowered in order to trigger a relative motion is higher than the kinetic friction force when the relative motion is different from zero. The switching function in this case is

$$\sigma(\mathbf{x}) = \dot{q}_{mid} - v_{ground}, \tag{40}$$

which splits the phase space according to the relative motion between the beam element at the midpoint and the moving belt. Interestingly, the difference between static and dynamic friction forces causes the fixed points of the positive and negative systems to be unstable under certain parameter values, triggering a limit cycle. Also in this case both crossing and sticking are allowed: the presence of sticking to the switching surface represents indeed a crucial factor in sustaining the limit cycle.

The data-driven procedure for the computation of the reduced order model is similar for all three piecewise-smooth systems. We constructed two different slow SSMs in each case, one for each region Σ^+ and Σ^-. Within each of these regions, the beam equations are analytic and hence the SSMs are approximated by a convergent Taylor expansion near the respective equilibrium points. We generate decaying trajectories which serve as training data, under $\mathbf{f}^+$ and $\mathbf{f}^-$, separately. The initial condition

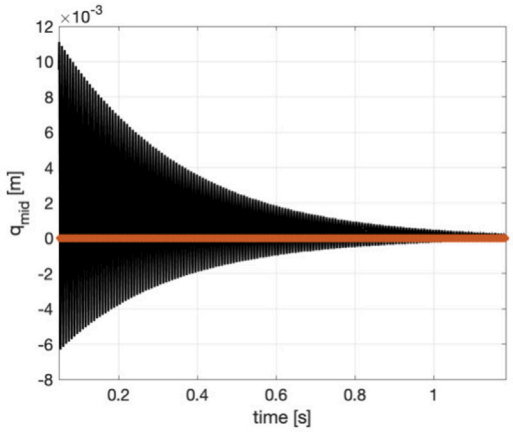

Fig. 9. Decaying trajectory of the von-Kármán beam with soft-impact located at the midpoint. The orange line refers to the switching between the two sub-regions. (For interpretation of the references to color in this figure legend, the reader is referred to the web version of this article.)

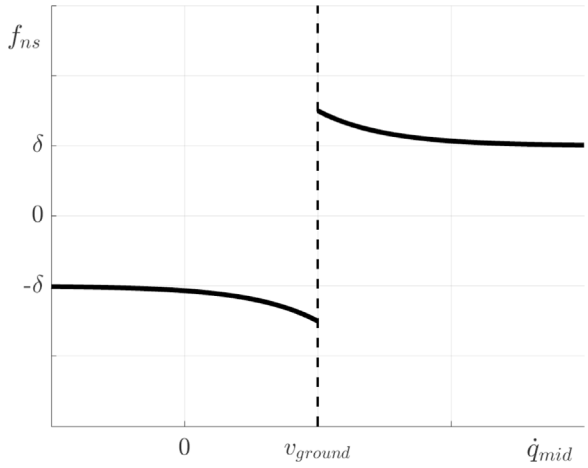

Fig. 10. Friction law dependent on the relative velocity between the midpoint of the von Kármán beam and the moving belt. In contrast to the Coulomb friction model, here the static friction force is different from the dynamic one.

is a deformed configuration caused by transverse static loading of 12 kN at the midpoint.

We seek a two-dimensional SSM, approximated by a 5th-order expansion and a 5th-order approximation of the reduced dynamics. According to Whitney's embedding theorem [37], the minimal embedding dimension for a two-dimensional SSM is $p = 5$, which is satisfied for our specific case, as we observe the full system. The error of the reconstructed SSM-based reduced model is quantified by the normalized mean-trajectory error (NMTE, see Cenedese et al. [21]) for each region Σ^+ and Σ^-. For a data set of P instances of observable points $\mathbf{y}_j \in \mathbb{R}^p$ and their reconstruction $\hat{\mathbf{y}}_j$:

$$\text{NMTE} = \frac{1}{\|\underline{\mathbf{y}}\|}\frac{1}{P}\sum_{j=1}^{P}\|\mathbf{y}_j - \hat{\mathbf{y}}_j\|, \tag{41}$$

where $\underline{\mathbf{y}}$ is a relevant normalization vector. Finally, we combine the two SSM-based reduced models according to their individual ranges of validity dictated by the switching function. We then employ the model trained on decaying trajectories to predict unforced trajectories (see Fig. 11) and force response. Based on the arguments of Cenedese et al. [21], moderate forcing terms can simply be added to the reduced model constructed from unforced data. Here, we consider a transversal periodic forcing applied to the midpoint. As seen in Fig. 12 for the

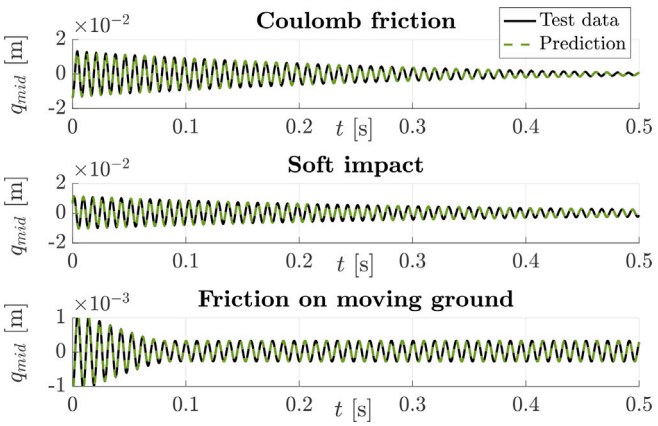

Fig. 11. Model-testing trajectories of the unforced von Kármán beam with different kinds of non-smoothness, and their reconstructions from an unforced, nonsmooth, SSM-based model. (For interpretation of the references to color in this figure legend, the reader is referred to the web version of this article.)

Coulomb friction and soft impact cases, the piecewise-smooth reduced order model closely tracks the response for a range of frequencies around the first mode of the system, even when the effect of the non-smoothness factor $\tilde{\delta}$ is not negligible. Increasing $\tilde{\delta}$ intensifies the dissipation in the system, entailing a lower amplitude of the response. In the soft impact case, $\tilde{\delta}$ strengthens the stiffness in some operating region, which leads to an overall shift of the resonance toward higher frequencies.

Modeling the sticking regime is delicate, as the constraints confining the trajectory within the switching surface must be enforced. This becomes especially relevant when the dynamics enter and exit the sticking regime multiple times, as in the case of the limit cycle that characterizes the beam with friction on moving ground, for a range of parameters. Since the condition for the sticking regime to occur is expressed in terms of physical variables, choosing the physical coordinates (vertical displacement and velocity at the midpoint) as the reduced variables for the SSM parametrization is advantageous. This is not the standard choice, as we usually employ a pair of coordinates spanning the slowest spectral subspace in order to describe a two-dimensional SSM. More details are given in the Appendix B. Let us consider a configuration of parameters wherein the limit cycle is triggered for the autonomous system already: adding forcing in this case generates an invariant periodic or quasiperiodic torus. The behavior of the response depends on the relationship between the frequency of the limit cycle of the autonomous system (f_{LC}) and that of the forcing term (f_F). In Fig. 13 we report the case for $f_F/f_{LC} = 1.125$, where the reduced order model (in green) is able to accurately capture the multi-frequency periodic solution of the full order system (in black).

5. Conclusions

We have presented an SSM-based model reduction procedure applicable to nonlinear, piecewise smooth dynamical systems. More specifically, we apply the classic SSM theory separately to different regions of the phase space where the system is smooth. Proper matching conditions are then enforced as crossing between those regions occurs.

The method proposed here accurately captured the piecewise smooth dynamics in both equation- and data-driven examples. The equation-driven examples included forced and unforced versions of a 2-DOF nonlinear oscillator with Coulomb friction. In this case, the SSMs involved were computed analytically.

The data-driven examples included forced and unforced von Kármán beam models with different types of piecewise smooth elements at their midpoints. In this case, the SSMs involved were calculated

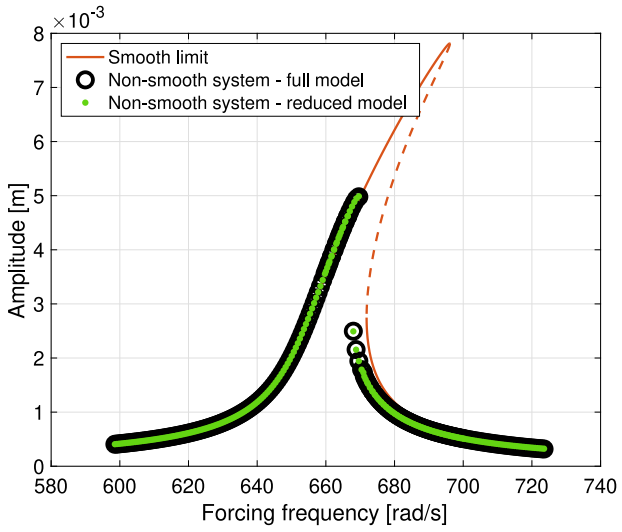

(a) Coulomb friction, $\tilde{\delta} = 1 \cdot 10^{-3}$

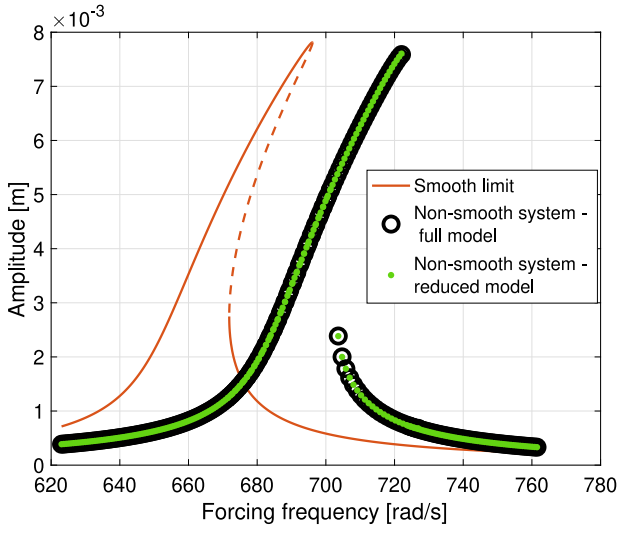

(b) soft impact, $\tilde{\delta} = 5 \cdot 10^{-4}$

Fig. 12. Response curves for the von Kármán beam forced periodically at the midpoint with Coulomb friction (a) and soft impact (b) with the same forcing level (35 kN). In both cases, the effect of non-smoothness is evident. The smooth case ($\tilde{\delta} = 0$) and full model cases are computed via the continuation software COCO [36], while the response of the reduced model is retrieved by numerical integration.

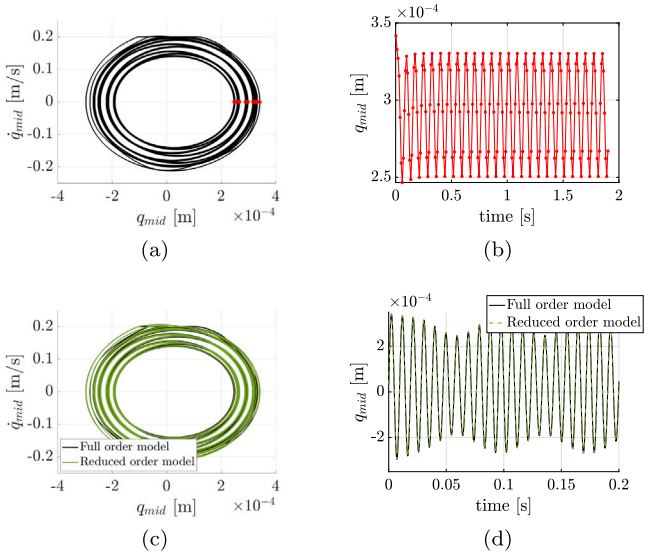

Fig. 13. Periodic orbit lying on a torus generated by external forcing ($50N$, $f_F/f_{LC} = 1.125$) applied to a von Kármán beam with friction on a moving ground, with unstable slowest eigenvalues. Fig. (b) shows the temporal history of the red dots in Fig. (a). Figs. (c) and (d) compare the reduced-order model (in green) with the full order one (in black). (For interpretation of the references to color in this figure legend, the reader is referred to the web version of this article.)

using an extended version of the SSMLearn algorithm. Not only did the piecewise-smooth reduced order model correctly capture single trajectories for all these different sources of non-smoothness, but it also accurately predicted the forced response. When the sticking regime played a crucial role in the system dynamics (a limit cycle existed for the beam with friction on moving ground), we proposed a specific parametrization of the SSMs based on physical coordinates. We did this to automatically verify the sticking conditions, as they are expressed in those coordinates.

In the present work, we assumed that the phase space is split in two regions, where the system is smooth. We then applied SSM reduction procedure with only one switching surface. In principle, the same procedure can be generalized to multiple switching surfaces, but it would require a careful choice of the reduced physical coordinates for the parametrization of SSMs. Indeed, if one wants to correctly track the sticking regime to different switching surfaces, different relevant physical coordinates might be needed. A further limitation of our method is the assumed smallness of the normalized non-smoothness parameter, for which the two equilibria, and hence their respective SSMs, lie close to each other.

Possible future work could investigate a more invasive effect of non-smooth elements to the system dynamics. In such a case, the condition relating points across a switching surface we have presented might not be able to furnish a proper initial condition in order for the reduced trajectory to synchronize with the solution of the full system. A new strategy taking into account the dynamics normal to the SSMs may then be required.

Code availability

The code supporting the results of this work is publicly available at https://github.com/haller-group/SSMLearn.

CRediT authorship contribution statement

Leonardo Bettini: Writing – review & editing, Writing – original draft, Software, Investigation. **Mattia Cenedese:** Software, Investigation, Conceptualization. **George Haller:** Writing – review & editing, Supervision, Project administration, Investigation, Conceptualization.

Declaration of competing interest

The authors declare that they have no known competing financial interests or personal relationships that could have appeared to influence the work reported in this paper.

Data availability

The data discussed in this work are publicly available at https://github.com/haller-group/SSMLearn.

Table A.1
Coefficients of the graph-style parametrization for the positive case.

	(2,0)	(1,1)	(0,2)	(3,0)	(2,1)	(1,2)	(0,3)
h_1^+	$8.2\ 10^{-3}$	$-2.4\ 10^{-2}$	$-7.3\ 10^{-3}$	$2.7\ 10^{-2}$	$-1.5\ 10^{-3}$	$2.3\ 10^{-3}$	$-1\ 10^{-3}$
h_2^+	$1.5\ 10^{-2}$	$1.7\ 10^{-2}$	$-2.8\ 10^{-3}$	$3.4\ 10^{-3}$	$4.6\ 10^{-2}$	$7.2\ 10^{-3}$	$3.2\ 10^{-2}$

Table A.2
Coefficients of the graph-style parametrization for the negative case.

	(2,0)	(1,1)	(0,2)	(3,0)	(2,1)	(1,2)	(0,3)
h_1^+	$-8.2\ 10^{-3}$	$2.4\ 10^{-2}$	$7.3\ 10^{-3}$	$2.7\ 10^{-2}$	$-1.5\ 10^{-3}$	$2.3\ 10^{-3}$	$-1\ 10^{-3}$
h_2^+	$-1.5\ 10^{-2}$	$-1.7\ 10^{-2}$	$2.8\ 10^{-3}$	$3.4\ 10^{-3}$	$4.6\ 10^{-2}$	$7.2\ 10^{-3}$	$3.2\ 10^{-2}$

Appendix A. Piecewise smooth systems

A.1. Filippov's closure for piecewise-smooth systems

In order to extend the validity of the governing Eqs. (4) to the switching surface Σ, we define an extended system, according to the Filippov's convex inclusion method

$$\dot{\mathbf{x}} \in \mathbf{F}(\mathbf{x}) = \begin{cases} \mathbf{f}^+(\mathbf{x}), & \mathbf{x} \in \Sigma^+ \\ \overline{\text{co}}\ \{\mathbf{f}^-(\mathbf{x}), \mathbf{f}^+(\mathbf{x})\} & \mathbf{x} \in \Sigma \\ \mathbf{f}^-(\mathbf{x}), & \mathbf{x} \in \Sigma^-, \end{cases} \tag{A.1}$$

where

$$\overline{\text{co}}\,\{\mathbf{f}^-, \mathbf{f}^+\} = \left\{ \frac{1+\lambda}{2}\mathbf{f}^+ + \frac{1-\lambda}{2}\mathbf{f}^-, \lambda \in [-1,1] \right\}. \tag{A.2}$$

Filippov's inclusion allows us to derive a model for the dynamics within the switching surface Σ. Indeed, exploiting the invariance relationship $\dot{\sigma}(\mathbf{x}) = 0 = \nabla\sigma \cdot \dot{\mathbf{x}} = 0$, we obtain

$$\lambda^{\Sigma} = \frac{(\mathbf{f}^- + \mathbf{f}^+) \cdot \nabla\sigma}{(\mathbf{f}^- - \mathbf{f}^+) \cdot \nabla\sigma}, \tag{A.3}$$

and hence Eq. (6).

A.2. Model reduction strategy

We recall some fundamental concepts about primary smooth SSMs and their relevance for model reduction (Haller and Ponsioen [7]). Restricting ourselves to a single region in which governing equations are smooth, we write

$$\begin{aligned} \dot{\mathbf{x}} = \mathbf{f}(\mathbf{x}, \boldsymbol{\Omega} t; \epsilon) &= \mathbf{A}\mathbf{x} + \mathbf{f}_0 + \epsilon \mathbf{f}_1(\mathbf{x}, \boldsymbol{\Omega} t), \\ \mathbf{f}_0(\mathbf{x}) &= \mathcal{O}(|\mathbf{x}|^2), \quad 0 \le \epsilon \ll 1, \end{aligned} \tag{A.4}$$

where $\mathbf{A} \in \mathbb{R}^n$ is the constant matrix of the linear part, $\mathbf{f}_0 : \mathbb{R}^n \to \mathbb{R}^n$ and $\mathbf{f}_1 : \mathbb{R}^n \times \mathbb{T}^l \to \mathbb{R}^n$, where $\mathbb{T}^l = S^1 \times \cdots \times S^l$ is the l-dimensional torus and with $\mathbf{f}_0, \mathbf{f}_1$ being class C^r functions. The degree of smoothness of the right-hand side is $r \in \mathbb{N}^+ \cup \{\infty, a\}$, where a refers to analyticity. The eigenvalues $\lambda_j = \alpha_j + i\omega_j \in \mathbb{C}$ of $\mathbf{A}$ are counted with their multiplicities and addressed in descending order according to their real part

$$\text{Re}\lambda_n \le \text{Re}\lambda_{n-1} \le \ldots \le \text{Re}\lambda_1 < 0. \tag{A.5}$$

The real and imaginary parts of the eigenvectors or generalized eigenvectors of $\mathbf{A}$ relative to the jth eigenvalue gives rise to the jth real modal subspace $E_j \subset \mathbb{R}^n$. The direct sum of modal subspaces defines a spectral subspace

$$E_{j_1,\ldots,j_q} = E_{j_1} \oplus E_{j_2} \oplus \cdots \oplus E_{j_q}. \tag{A.6}$$

If we further assume that $\text{Re}\lambda_j < 0\,\forall j$, projecting the linearized system onto the nested hierarchy of slow spectral subspaces

$$E^1 \subset E^2 \subset \ldots, \quad E^k := E_{1,\ldots,k} \text{ for } k = 1, \ldots, n \tag{A.7}$$

defines a strategy for reducing the order of the linearized dynamics with increasing accuracy as k is increased (Galerkin projection method). We want now to study the existence of a nonlinear continuation of such a spectral subspace, in order to be able to reduce the order of the model, but in the presence of nonlinear and also time-dependent terms. In particular, let us fix a specific spectral subspace $E = E_{j_1,\ldots,j_q}$. If the non-resonance condition

$$\langle m, \text{Re}\lambda \rangle_E \neq \text{Re}\lambda_l, \quad \lambda_l \notin \text{Spect}(A|_E), \quad 2 \le |m| \le \Sigma(E) \tag{A.8}$$

holds, then infinitely many nonlinear continuations of E exist, for ϵ small enough (Haller et al. [14]). Here $|m| := \sum_{j=1}^q m_j$. In (A.8), $\Sigma(E)$ is the absolute spectral quotient defined as

$$\Sigma(E) = \text{Int}\left[\frac{\min\limits_{\lambda \in \text{Spect}(A) - \text{Spect}(A|_E)} \text{Re}\lambda}{\max\limits_{\lambda \in \text{Spect}(A|_E)} \text{Re}\lambda} \right]. \tag{A.9}$$

Among all $C^{\Sigma(E)+1}$ invariant manifolds there is a unique smoothest one, the primary SSM $\mathcal{W}(E)$, which can therefore be approximated more accurately than the other infinitely many nonlinear continuations of E. In the case of autonomous systems ($\epsilon = 0$), the non-resonance condition can be relaxed to

$$\langle m, \lambda \rangle_E \neq \lambda_l, \quad \lambda_l \notin \text{Spect}(A|_E), \quad 2 \le |m| \le \sigma(E), \tag{A.10}$$

where $\sigma(E)$ is the relative spectral quotient, defined as

$$\sigma(E) = \text{Int}\left[\frac{\min\limits_{\lambda \in \text{Spect}(A)} \text{Re}\lambda}{\max\limits_{\lambda \in \text{Spect}(A|_E)} \text{Re}\lambda} \right]. \tag{A.11}$$

A.3. Equation-driven model reduction for the Shaw-Pierre model

Once we obtain the governing equations of the system centered at the two fixed points $\mathbf{x}_0^{\pm}$ (Eq. (25)), we perform a linear change of coordinates,

$$\boldsymbol{\xi}^{\pm} = \mathbf{V}\boldsymbol{\eta}^{\pm}, \tag{A.12}$$

where

$$\boldsymbol{\eta}^{\pm} = (\mathbf{y}^{\pm}, \mathbf{z}^{\pm}) \in E_1 \times E_2$$

and $\mathbf{V}$ is the matrix composed of the eigenvectors of $\tilde{\mathbf{A}_0}$ as columns. For ease of notation, the superscript $\pm$ is dropped in the following equations. The equations of motion now read

$$\begin{aligned} \dot{\mathbf{y}} = \tilde{\mathbf{A}}_{\mathbf{y}}\mathbf{y} + \left(\mathbf{r}\,\mathbf{f}_{\mathbf{nl}}^{\mathbf{III}}\right)_{\mathbf{y}} \pm \left(\mathbf{r}\,\mathbf{f}_{\mathbf{nl}}^{\mathbf{II}}\right)_{\mathbf{y}} &= \begin{pmatrix} -0.0789 & 1.0342 \\ -1.0342 & -0.0789 \end{pmatrix} \mathbf{y} \\ &+ \begin{pmatrix} 0.9968 \\ -0.0761 \end{pmatrix} q^{III}(\boldsymbol{\eta}) \pm \begin{pmatrix} 0.9968 \\ -0.0761 \end{pmatrix} q^{II}(\boldsymbol{\eta}) \end{aligned} \tag{A.13}$$

and

$$\begin{aligned} \dot{\mathbf{z}} = \tilde{\mathbf{A}}_{\mathbf{z}}\mathbf{z} + \left(\mathbf{r}\,\mathbf{f}_{\mathbf{nl}}^{\mathbf{III}}\right)_{\mathbf{z}} \pm \left(\mathbf{r}\,\mathbf{f}_{\mathbf{nl}}^{\mathbf{II}}\right)_{\mathbf{z}} &= \begin{pmatrix} -0.3711 & 1.6987 \\ -1.6987 & -0.3711 \end{pmatrix} \mathbf{z} \\ &+ \begin{pmatrix} -0.8278 \\ 0.1808 \end{pmatrix} q^{III}(\boldsymbol{\eta}) \pm \begin{pmatrix} -0.8278 \\ 0.1808 \end{pmatrix} q^{II}(\boldsymbol{\eta}), \end{aligned} \tag{A.14}$$

where

$$q^{III}(\boldsymbol{\eta}) = -\frac{1}{2}(0.1645 z_1 + 0.3070 z_2 + 0.0441 y_1 - 0.4828 y_2)^3$$

and

$$q^{II}(\boldsymbol{\eta}) = \frac{3}{2} q_0 (0.1645 z_1 + 0.3070 z_2 + 0.0441 y_1 - 0.4828 y_2)^2.$$

For each case, we seek a cubic Taylor expansion as an approximation of the slow primary SSM anchored at $\boldsymbol{\xi}^{\pm} = 0$ in the form

$$\mathbf{z} = \sum_{|\mathbf{p}|=2}^{3} \mathbf{h}_{\mathbf{p}} \mathbf{y}^{\mathbf{p}}, \qquad \mathbf{p} = (p_1, p_2) \in \mathbb{N}^2, \tag{A.15}$$

Table A.3
Coefficients of the reduced dynamics for the positive case.

	(1,0)	(0,1)	(2,0)	(1,2)	(0,2)	(3,0)	(2,1)	(1,2)	(0,3)
r_1^+	−0.074	1.004	1.4 10^{-4}	3.8 10^{-3}	2.6 10^{-2}	−1.8 10^{-5}	4.5 10^{-4}	1.4 10^{-2}	6.5 10^{-2}
r_2^+	−1.004	−0.074	−3.0 10^{-5}	−8.1 10^{-4}	−5.5 10^{-3}	3.9 10^{-6}	−9.7 10^{-5}	−3.1 10^{-3}	−1.4 10^{-2}

Table A.4
Coefficients of the reduced dynamics for the negative case.

	(1,0)	(0,1)	(2,0)	(1,2)	(0,2)	(3,0)	(2,1)	(1,2)	(0,3)
r_1^+	−0.074	1.004	−1.4 10^{-4}	−3.8 10^{-3}	−2.6 10^{-2}	−1.8 10^{-5}	4.5 10^{-4}	1.4 10^{-2}	6.5 10^{-2}
r_2^+	−1.004	−0.074	3.0 10^{-5}	8.1 10^{-4}	5.5 10^{-3}	3.9 10^{-6}	−9.7 10^{-5}	−3.1 10^{-3}	−1.4 10^{-2}

where

$$\mathbf{y}^{\mathbf{p}} = y_1^{p_1}\, y_2^{p_2}, \qquad \mathbf{h}_{\mathbf{p}} = \begin{pmatrix} h_{1,\mathbf{p}} \\ h_{2,\mathbf{p}} \end{pmatrix} \in \mathbb{R}^2.$$

The expanded formula is reported in Eq. (A.16) below:

$$\begin{cases} z_1^{\pm} = h_1^{\pm,(2,0)} y_1^2 + h_1^{\pm,(1,1)} y_1 y_2 + h_1^{\pm,(0,2)} y_2^2 \\ \quad + h_1^{\pm,(3,0)} y_1^3 + h_1^{\pm,(2,1)} y_1^2 y_2 + h_1^{\pm,(1,2)} y_1^1 y_2^2 \\ \quad + h_1^{\pm,(0,3)} y_2^3, \\ z_2^{\pm} = h_2^{\pm,(2,0)} y_1^2 + h_2^{\pm,(1,1)} y_2 y_2 + h_2^{\pm,(0,2)} y_2^2 \\ \quad + h_2^{\pm,(3,0)} y_1^3 + h_2^{\pm,(2,1)} y_1^2 y_2 + h_2^{\pm,(1,2)} y_1^1 y_2^2 \\ \quad + h_2^{\pm,(0,3)} y_2^3. \end{cases} \tag{A.16}$$

Also the reduced dynamics can be written in the form of a Taylor expansion:

$$\begin{cases} r_1^{\pm} = r_1^{\pm,(1,0)} y_1 + r_1^{\pm,(0,1)} y_2 + r_1^{\pm,(2,0)} y_1^2 + r_1^{\pm,(1,1)} y_1 y_2 \\ \quad + r_1^{\pm,(0,2)} y_2^2 + r_1^{\pm,(3,0)} y_1^3 + r_1^{\pm,(2,1)} y_1^2 y_2 \\ \quad + r_1^{\pm,(1,2)} y_1^1 y_2^2 + r_1^{\pm,(0,3)} y_2^3 \\ r_2^{\pm} = r_2^{\pm,(1,0)} y_1 + r_2^{\pm,(0,1)} y_2 + r_2^{\pm,(2,0)} y_1^2 + r_2^{\pm,(1,1)} y_2 y_2 \\ \quad + r_2^{\pm,(0,2)} y_2^2 + r_2^{\pm,(3,0)} y_1^3 + r_2^{\pm,(2,1)} y_1^2 y_2 \\ \quad + r_2^{\pm,(1,2)} y_1^1 y_2^2 + r_2^{\pm,(0,3)} y_2^3. \end{cases} \tag{A.17}$$

The invariance equation on the primary SSM reads

$$\begin{aligned} & D_y \mathbf{h}(\mathbf{y})\, A_y\, \mathbf{y} + D_y \mathbf{h}(\mathbf{y})\, \mathbf{r}_y \left[q^{III}(\mathbf{y}, \mathbf{h}(\mathbf{y})) \pm q^{II}(\mathbf{y}, \mathbf{h}(\mathbf{y})) \right] \\ & \quad = A_z\, \mathbf{h}(\mathbf{y}) + \mathbf{r}_z \left[q^{III}(\mathbf{y}, \mathbf{h}(\mathbf{y})) \pm q^{II}(\mathbf{y}, \mathbf{h}(\mathbf{y})) \right]. \end{aligned} \tag{A.18}$$

Equating powers of $\mathbf{y}$ leads to a set of linear equations with the parametrization coefficients as unknowns ((A.19) and (A.20)) that can be solved as long as nonresonance conditions are satisfied. The values of the coefficients in (A.16) and (A.17) are reported in Tables A.1, A.2, A.3 and A.4, for $\delta = 0.1$.

$$\mathcal{O}(2,0): \quad D_y \mathbf{h}^{(2)} A_y \mathbf{y} = A_z \mathbf{h}^{(2)} \pm \mathbf{r}_z q^{II,(2)}$$

$$\begin{cases} a_1 \left(2\mathrm{Re}(\lambda_1) - \mathrm{Re}(\lambda_2)\right) - a_2 \mathrm{Im}(\lambda_1) - b_1 \mathrm{Im}(\lambda_2) \\ \quad = \pm 3\alpha q_0 r_{z,1} p_3^2 \\ a_2 \left(2\mathrm{Re}(\lambda_1) - \mathrm{Re}(\lambda_2)\right) + 2a_1 \mathrm{Im}(\lambda_1) - 2a_3 \mathrm{Im}(\lambda_1) \\ \quad - b_2 \mathrm{Im}(\lambda_2) = \pm 6\alpha p_3 p_4 q_0 r_{z,1} \\ a_3 \left(2\mathrm{Re}(\lambda_1) - \mathrm{Re}(\lambda_2)\right) + a_2 \mathrm{Im}(\lambda_1) - b_3 \mathrm{Im}(\lambda_2) \\ \quad = \pm 3\alpha q_0 r_{z,1} p_4^2 \\ b_1 \left(2\mathrm{Re}(\lambda_1) - \mathrm{Re}(\lambda_2)\right) + a_1 \mathrm{Im}(\lambda_2) - b_2 \mathrm{Im}(\lambda_1) \\ \quad = \pm 3\alpha q_0 r_{z,2} p_3^2 \\ b_2 \left(2\mathrm{Re}(\lambda_1) - \mathrm{Re}(\lambda_2)\right) + a_2 \mathrm{Im}(\lambda_2) + 2b_1 \mathrm{Im}(\lambda_1) \\ \quad - 2b_3 \mathrm{Im}(\lambda_1) = \pm 6\alpha p_3 p_4 q_0 r_{z,2} \\ b_3 \left(2\mathrm{Re}(\lambda_1) - \mathrm{Re}(\lambda_2)\right) + a_3 \mathrm{Im}(\lambda_2) + b_2 \mathrm{Im}(\lambda_1) \\ \quad = \pm 3\alpha q_0 r_{z,2} p_4^2 \end{cases} \tag{A.19}$$

$$\mathcal{O}(3,0): \quad D_y \mathbf{h}^{(3)} A_y \mathbf{y} \pm D_y \mathbf{h}^{(2)} \mathbf{r}_y q^{II,(2)} = A_z \mathbf{h}^{(3)} + \mathbf{r}_z \left(q^{III,(3)} \pm q^{II,(3)}\right)$$

$$\begin{cases} a_4 \left(3\mathrm{Re}(\lambda_1) - \mathrm{Re}(\lambda_2)\right) \mp r_{z,1}(6\alpha q_0 (a_1 p_1 + b_1 p_2) p_3) \\ \quad - a_5 \mathrm{Im}(\lambda_1) - b_4 \mathrm{Im}(\lambda_2) \pm 3\alpha p_3^2 q_0 (2a_1 r_{y,1} + a_2 r_{y,2}) \\ \quad = -r_{z,1} \alpha p_3^3 \\ a_5 \left(3\mathrm{Re}(\lambda_1) - \mathrm{Re}(\lambda_2)\right) + 3a_4 \mathrm{Im}(\lambda_1) - 2a_6 \mathrm{Im}(\lambda_1) \\ \quad - b_5 \mathrm{Im}(\lambda_2) \mp r_{z,1}(3\alpha q_0 (2p_4 (a_1 p_1 + b_1 p_2) \\ \quad + 2p_3 (a_2 p_1 + b_2 p_2))) \pm 3\alpha p_3^2 q_0 (a_2 r_{y,1} + 2a_3 r_{y,2}) \\ \quad \pm 6\alpha p_3 p_4 q_0 (2a_1 r_{y,1} + a_2 r_{y,2}) = -r_{z,1} 3\alpha p_3^2 p_4 \\ a_6 \left(3\mathrm{Re}(\lambda_1) - \mathrm{Re}(\lambda_2)\right) + 2a_5 \mathrm{Im}(\lambda_1) - 3a_7 \mathrm{Im}(\lambda_1) \\ \quad - b_6 \mathrm{Im}(\lambda_2) \mp r_{z,1}(3\alpha q_0 (2p_4 (a_2 p_1 + b_2 p_2) \\ \quad + 2p_3 (a_3 p_1 + b_3 p_2))) \pm 3\alpha p_4^2 q_0 (2a_1 r_{y,1} + a_2 r_{y,2}) \\ \quad \pm 6\alpha p_3 p_4 q_0 (a_2 r_{y,1} + 2a_3 r_{y,2}) = -r_{z,1} 3\alpha p_3 p_4^2 \\ a_7 \left(3\mathrm{Re}(\lambda_1) - \mathrm{Re}(\lambda_2)\right) \mp r_{z,1}(6\alpha q_0 (a_3 p_1 + b_3 p_2) p_4) \\ \quad + a_6 \mathrm{Im}(\lambda_1) - b_7 \mathrm{Im}(\lambda_2) \pm 3\alpha p_4^2 q_0 (a_2 r_{y,1} + 2a_3 r_{y,2}) \\ \quad = -r_{z,1} \alpha p_4^3 \\ b_4 \left(3\mathrm{Re}(\lambda_1) - \mathrm{Re}(\lambda_2)\right) \mp r_{z,2}(6\alpha q_0 (a_1 p_1 + b_1 p_2) p_3) \\ \quad + a_4 \mathrm{Im}(\lambda_2) - b_5 \mathrm{Im}(\lambda_1) \pm 3\alpha p_3^2 q_0 (2b_1 r_{y,1} + b_2 r_{y,2}) \\ \quad = -r_{z,2} \alpha p_3^3 \\ b_5 \left(3\mathrm{Re}(\lambda_1) - \mathrm{Re}(\lambda_2)\right) + a_5 \mathrm{Im}(\lambda_2) + 3b_4 \mathrm{Im}(\lambda_1) \\ \quad - 2b_6 \mathrm{Im}(\lambda_1) \mp r_{z,2}(3\alpha q_0 (2p_4 (a_1 p_1 + b_1 p_2) \\ \quad + 2p_3 (a_2 p_1 + b_2 p_2))) \pm 3\alpha p_3^2 q_0 (b_2 r_{y,1} + 2b_3 r_{y,2}) \\ \quad \pm 6\alpha p_3 p_4 q_0 (2b_1 r_{y,1} + b_2 r_{y,2}) = -r_{z,2} 3\alpha p_3^2 p_4 \\ b_6 \left(3\mathrm{Re}(\lambda_1) - \mathrm{Re}(\lambda_2)\right) + a_6 \mathrm{Im}(\lambda_2) + 2b_5 \mathrm{Im}(\lambda_1) \\ \quad - 3b_7 \mathrm{Im}(\lambda_1) \mp r_{z,2}(3\alpha q_0 (2p_4 (a_2 p_1 + b_2 p_2) \\ \quad + 2p_3 (a_3 p_1 + b_3 p_2))) \pm 3\alpha p_4^2 q_0 (2b_1 r_{y,1} + b_2 r_{y,2}) \\ \pm 6\alpha p_3 p_4 q_0 (b_2 r_{y,1} \quad + 2b_3 r_{y,2}) = -r_{z,2} 3\alpha p_3 p_4^2 \\ b_7 \left(3\mathrm{Re}(\lambda_1) - \mathrm{Re}(\lambda_2)\right) \mp r_{z,2}(6\alpha q_0 (a_3 p_1 + b_3 p_2) p_4) \\ \quad + a_7 \mathrm{Im}(\lambda_2) + b_6 \mathrm{Im}(\lambda_1) \pm 3\alpha p_4^2 q_0 (b_2 r_{y,1} + 2b_3 r_{y,2}) \\ \quad = -r_{z,2} \alpha p_4^3 \end{cases} \tag{A.20}$$

A.3.1. Errors

Considering the positive case, we report in Fig. A.14 the relative errors between the dynamics of the full system and the reduced one. The initial condition is given slightly outside the SSM: the attracting properties of the SSM are evident as the error reduces significantly with time. Moreover, increasing the value of δ means intensifying the amplitude of the constant external forcing and therefore the error of the reduced dynamics is shifted upwards.

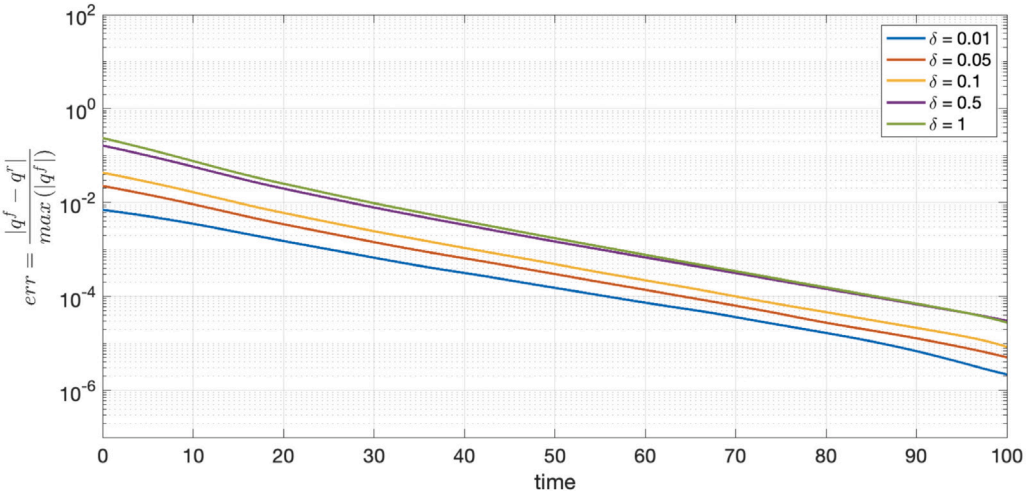

Fig. A.14. Relative error on the displacement of the first mass for different values of δ.

The invariance error represents the accuracy of the Taylor expansion in approximating the invariant manifold and the reduced dynamics computed on it. It is quantified as

$$E_{inv} = \frac{1}{N}\sum_{i=1}^{N}\frac{\|\text{LHS}(y_i) - \text{RHS}(y_i)\|_2}{\|\text{RHS}(y_i)\|_2}, \qquad y_i \in Y_s \subset D(\rho) = \{(y_1, y_2) \in \mathbb{R}^2 : \|y\| = \rho\}, \tag{A.21}$$

where LHS and RHS refer to the left-hand and right-hand sides of Eq. (A.18) and ρ denotes the distance from the fixed point in reduced coordinates (y_1, y_2) (see Fig. A.15).

A.3.2. Choice of initial conditions across SSMs

Fig. 5 shows how different strategies for enforcing continuity of certain physical variables across the switching surface affect the evolution of the reduced trajectory, when crossing occurs. The most effective strategy in tracking the full dynamics is the one corresponding to the red line in Fig. A.16, where no continuity constraint is enforced.

Assuming that the reduced trajectory jumps from the manifold $\mathcal{M}^+$ to $\mathcal{M}^-$, the final point on $\mathcal{M}^+$ is defined by

$$\boldsymbol{\eta}^+ = \left(\mathbf{y}^+, \mathbf{z}^+\right) \tag{A.22}$$

and corresponds to the physical coordinates

$$\mathbf{x} = \mathbf{V}\boldsymbol{\eta}^+ + \mathbf{x}_0^+. \tag{A.23}$$

The same physical coordinates can be described by the coordinates related to $\mathcal{M}^-$, namely,

$$\mathbf{x} = \mathbf{V}\boldsymbol{\eta}^- + \mathbf{x}_0^-. \tag{A.24}$$

Equating (A.23) and (A.24), we then obtain the relationship between the reduced coordinates (29).

This strategy has a clear geometric meaning: projecting the final point on one of the manifolds onto the other one gives a linear approximation of a stable fiber emanating from the second manifold. As a consequence, the new initial condition generates a trajectory on the second manifold that approximates the one to which the full trajectory converges the fastest. In contrast, the other possible approaches prioritize the continuity of physical coordinates without enhancing the approximation of the stable fiber. In other words, trajectories resulting form these other approaches do not improve the approximation of the one to which the trajectory of the full dynamics converges.

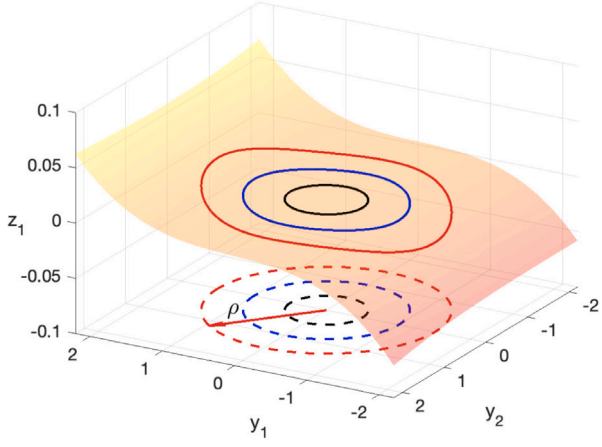

(a)

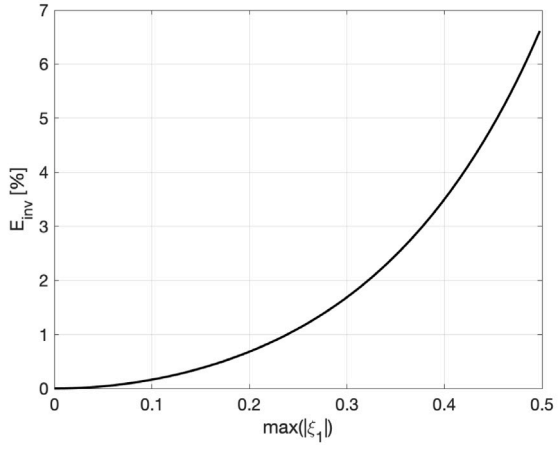

(b)

Fig. A.15. Invariance error for different values of distance from the fixed point $\mathbf{x}_0^+$. (For interpretation of the references to color in this figure legend, the reader is referred to the web version of this article.)

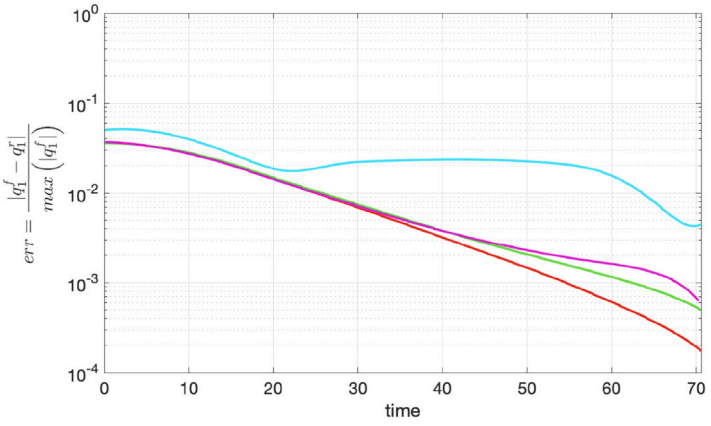

Fig. A.16. Relative errors between the solution of the reduced model according to the different strategies and the full model, evaluated for the displacement of the first mass and for $\delta = 10^{-3}$. The colors refer to the strategies depicted in Fig. 5: projection onto the new SSM (red), minimization of all physical variables (green), continuity of q_1 (purple) and continuity of both q_1 and q_2 (light blue). (For interpretation of the references to color in this figure legend, the reader is referred to the web version of this article.)

A.3.3. Approximation of Poincaré map and invariant set.

The Poincaré map of the full order model introduced in Section 3.3 can be approximated by exploiting information from the reduced-order model only. Since the invariant curve unveiled by the Poincaré map lies close to the intersection between the positive and negative SSMs and the switching surface (blue and red lines in Fig. A.17), the invariant set can be approximated by those curves up to specific points, $\tilde{x}^{\pm}_{edge}$, which need to be estimated and play the same role as $x^{\pm}_{edge}$ for the full order model. We call the average of the blue and red lines the centerline (dashed line in Fig. A.17).

Recalling that the preimages of $x^{\pm}_{edge}$ under the Poincaré map are the intersections of Γ with the gray surfaces ($x^{\pm}_{pre}$), we want to approximate such configurations for the reduced-order model as well ($\tilde{x}^{\pm}_{pre}$). The strategy is described for the computation of $\tilde{x}^{-}_{edge}$, but the same applies to $\tilde{x}^{+}_{edge}$. Referring to Fig. A.17, we consider the intersection of the centerline and that of the blue line with the gray surface. We take then the average of such intersections to obtain the light blue circle. Such a point is projected (light blue cross) onto the $\mathcal{M}^-$ (not shown in the figure), representing the initial condition sought. The reduced order model is then advected on $\mathcal{M}^-$ until the switching surface is hit, identifying $\tilde{x}^{-}_{edge}$. We note that this procedure requires information coming from the reduced-order model only.

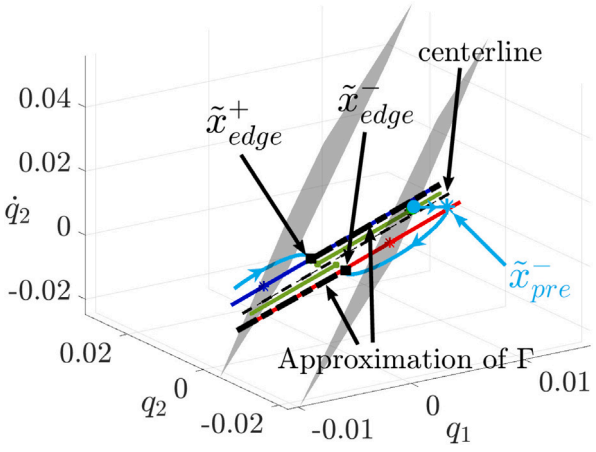

Fig. A.17. Approximation of the invariant set induced by the Poincaré map (piecewise continuous green line) exploiting information coming from the reduced order model only. (For interpretation of the references to color in this figure legend, the reader is referred to the web version of this article.)

A.3.4. Non-autonomous problem

The time-dependent SSMs related to the positive and negative cases are sought in the form of a cubic Taylor expansion

$$\mathbf{z} = \sum_{|\mathbf{p}|=2}^{3} \mathbf{h}_{\mathbf{p}} \mathbf{y}^{\mathbf{p}} + \epsilon \mathbf{h}_{\epsilon}(\Omega t), \qquad \mathbf{p} = (p_1, p_2) \in \mathbb{N}^2. \tag{A.25}$$

The invariance equation is now slightly modified to read

$$\begin{aligned} &D_y \mathbf{h}(\mathbf{y})\, A_y\, \mathbf{y} + D_y \mathbf{h}(\mathbf{y})\, \mathbf{r}_y \ \left[q^{III}(\mathbf{y}, \mathbf{h}(\mathbf{y})) \pm q^{II}(\mathbf{y}, \mathbf{h}(\mathbf{y}))\right] \\ &\quad + \epsilon \left(V^{-1} \mathbf{f}_{\epsilon}\right)_y + \epsilon D_t \mathbf{h}_{\epsilon} = A_z\, \mathbf{h}(\mathbf{y}) + \mathbf{r}_z \ \Big[q^{III}(\mathbf{y}, \mathbf{h}(\mathbf{y})) \\ &\quad \pm q^{II}(\mathbf{y}, \mathbf{h}(\mathbf{y})) \Big] + \epsilon \left(V^{-1} \mathbf{f}_{\epsilon}\right)_z . \end{aligned} \tag{A.26}$$

Collecting the terms of order ϵ, we obtain a set of ordinary differential equations, which can be solved by a Fourier representation of the periodic forcing and time dependent terms in the parametrization, whereby the forcing term becomes

$$\mathbf{h}_{\epsilon} = \sum_{n} \hat{\mathbf{h}}_{\epsilon,n} e^{in\Omega t} = \hat{\mathbf{h}}_{-1} e^{-i\Omega t} + \hat{\mathbf{h}}_{1} e^{i\Omega t}. \tag{A.27}$$

The reduced order model well reproduces the dynamics of the system, as long as the forcing amplitude ϵ remains small and the assumption of small friction coefficient holds. Fig. A.18 shows how the full trajectory rapidly approaches the reduced one, as the initial condition lies outside the primary SSM. They both eventually land on the attracting limit cycle induced by forcing. In particular, the rate at which the reduced-order model prediction converges to the full-order model trajectory is definitely greater than the rates at which the limit cycle is approached by both of them, which is then practically identical.

Appendix B. Parametrization of invariant manifolds

In this section, we recall some concepts for the construction of reduced order models with invariant manifolds in a data-driven setting. In particular, referring to [23], we show that one can choose arbitrary reduced coordinates, as long as they describe the invariant manifold as a graph. This justifies the choice of physical coordinates as reduced coordinates in the von Kármán beam example with friction on moving ground, as it allows us to check the sticking condition in a convenient way .

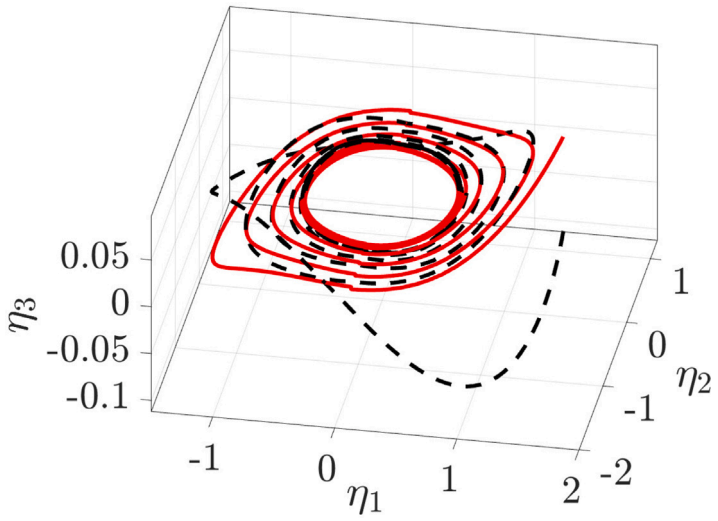

Fig. A.18. Trajectories of the full (black dashed) and reduced (red) models in modal coordinates (η_1, η_2, η_3), starting from the initial condition $\mathbf{x}_0 = (0, 0, 0.76, 0.76)$, with friction coefficient $\delta = 10^{-2}$ and forcing parameter $\epsilon = 10^{-1}$.

In the setting of Eq. (A.4), we consider a generic spectral subspace

$$E^{2q} = E_{j_1} \oplus E_{j_2} \oplus \cdots \oplus E_{j_q}, \tag{B.1}$$

and denote as $\mathrm{Spectr}(\mathbf{A}|_{E^{2q}})$ the set of the eigenvalues related to E^{2q}. This spectral subspace can be represented by the span of the eigenvectors of $\mathbf{A}|_{E^{2q}}$. The eigenvectors are collected as columns of the matrix $\mathbf{V}_{E^{2q}} \in \mathbb{C}^{2n\times 2q}$ satisfying $\mathbf{A}\mathbf{V}_{E^{2q}} = \mathbf{V}_{E^{2q}}\mathbf{R}_{E^{2q}}$, where $\mathbf{R}_{E^{2q}}$ is a diagonal matrix containing $\mathrm{Spectr}(\mathbf{A}|_{E^{2q}})$ as diagonal. Matrix $\mathbf{V}_{E^{2q}}$ defines also its adjoint $\mathbf{W}_{E^{2q}} \in \mathbb{C}^{2q\times 2n}$, such that $\mathbf{W}_{E^{2q}}\mathbf{A} = \mathbf{R}_{E^{2q}}\mathbf{W}_{E^{2q}}$ and normalized according to $\mathbf{W}_{E^{2q}}\mathbf{V}_{E^{2q}} = \mathbf{I}$. Assuming that the spectral subspace E^{2q} satisfies the nonresonance conditions (A.8), then the phase space is characterized by SSMs tangent to E^{2q}, among which the primary one is the smoothest and addressed as $\mathcal{W}(E^{2q})$. If we want to study the dynamics on the manifold $\mathcal{W}(E^{2q})$, we need the coordinate chart $\mathbf{y} = \mathbf{w}(\mathbf{x}, \boldsymbol{\Omega}\mathbf{t}; \epsilon)$ and its inverse, i.e. the parametrization of the manifold $\mathbf{x} = \mathbf{v}(\mathbf{y}, \boldsymbol{\Omega}t; \epsilon)$

$$\mathbf{y} = \mathbf{w}(\mathbf{v}(\mathbf{y}, \boldsymbol{\Omega}t; \epsilon), \boldsymbol{\Omega}\mathbf{t}; \epsilon), \quad \mathbf{x} = \mathbf{v}(\mathbf{w}(\mathbf{x}, \boldsymbol{\Omega}\mathbf{t}; \epsilon), \boldsymbol{\Omega}\mathbf{t}; \epsilon). \tag{B.2}$$

Hence, the reduced dynamics read

$$\dot{\mathbf{y}} = \mathbf{r}(\mathbf{y}, \boldsymbol{\Omega}t; \epsilon). \tag{B.3}$$

Since the mappings $\mathbf{v}, \mathbf{w}$ are invariant under the full and the reduced dynamics $\mathbf{f}$ and $\mathbf{r}$, we write

$$\begin{cases} D_{\mathbf{y}}\mathbf{v}(\mathbf{y}, \boldsymbol{\Omega}t; \epsilon)\,\mathbf{r}(\mathbf{y}, \boldsymbol{\Omega}t; \epsilon) + D_t\mathbf{v}(\mathbf{y}, \boldsymbol{\Omega}t; \epsilon) \\ \quad = \mathbf{f}(\mathbf{v}(\mathbf{y}, \boldsymbol{\Omega}t; \epsilon), \boldsymbol{\Omega}t; \epsilon), \\ D_{\mathbf{x}}\mathbf{w}(\mathbf{x}, \boldsymbol{\Omega}t; \epsilon)\,\mathbf{f}(\mathbf{x}, \boldsymbol{\Omega}t; \epsilon) + D_t\mathbf{w}(\mathbf{x}, \boldsymbol{\Omega}t; \epsilon) \\ \quad = \mathbf{r}(\mathbf{w}(\mathbf{x}, \boldsymbol{\Omega}t; \epsilon), \boldsymbol{\Omega}t; \epsilon). \end{cases} \tag{B.4}$$

Moreover, as the SSM depends smoothly on the parameter ϵ, we seek the expansions for $\mathbf{w}, \mathbf{v}$ and $\mathbf{r}$ in the form

$$\begin{cases} \mathbf{w}(\mathbf{x}, \boldsymbol{\Omega}t; \epsilon) = \mathbf{W}_0 + \mathbf{w}_{nl}(\mathbf{x}) + \epsilon\mathbf{w}_1(\boldsymbol{\Omega}t) + \mathcal{O}(\epsilon\|\mathbf{x}\|), \\ \mathbf{v}(\mathbf{y}, \boldsymbol{\Omega}t; \epsilon) = \mathbf{V}_0 + \mathbf{v}_{nl}(\mathbf{y}) + \epsilon\mathbf{v}_1(\boldsymbol{\Omega}t) + \mathcal{O}(\epsilon\|\mathbf{y}\|), \\ \mathbf{r}(\mathbf{y}, \boldsymbol{\Omega}t; \epsilon) = \mathbf{R}_0 + \mathbf{r}_{nl}(\mathbf{y}) + \epsilon\mathbf{r}_1(\boldsymbol{\Omega}t) + \mathcal{O}(\epsilon\|\mathbf{y}\|), \end{cases} \tag{B.5}$$

with $\mathbf{W}_0 \in \mathbb{C}^{2q\times 2n}$, $\mathbf{V}_0 \in \mathbb{C}^{2n\times 2q}$ and $\mathbf{R}_0 \in \mathbb{C}^{2q\times 2q}$ and such that $\mathrm{range}(\mathbf{V}_0) = E^{2q}$ and $\mathrm{Spectr}(\mathbf{R}_0) = \mathrm{Spectr}(\mathbf{A}|_{E^{2q}})$. Substituting the expansions (B.5) into (B.2) and taking the linear contributions for $\epsilon = 0$, we obtain

$$\mathbf{W}_0\mathbf{V}_0 = \mathbf{I}, \tag{B.6}$$

while considering Eqs. (B.4) gives:

$$\mathbf{W}_0\mathbf{A}\mathbf{V}_0 = \mathbf{R}_0. \tag{B.7}$$

Since the spectra of $\mathbf{R}_0$ and that of $\mathbf{A}$ are the same,

$$\mathbf{R}_0 = \mathbf{P}\mathbf{R}_{E^{2q}}\mathbf{P}^{-1}, \tag{B.8}$$

holds, which, coupled with Eq. (B.7), yields:

$$\mathbf{W}_0 = \mathbf{P}\mathbf{W}_{E^{2q}} \quad \text{and} \quad \mathbf{V}_0 = \mathbf{V}_{E^{2q}}\mathbf{P}^{-1}. \tag{B.9}$$

In principle, the coordinate chart can be arbitrarily chosen as a projection to the reduced coordinates defined by $\mathbf{W}_0$, as long as it is able to describe the manifold as a graph. In other words, once we define $\mathbf{W}_0$ and we know the eigenvectors spanning the tangent plane to the manifold $V_{E^{2q}}$, then from (B.6) and the second relation of (B.9) we compute the matrix $\mathbf{P}$ as

$$\mathbf{P} = \mathbf{W}_0\mathbf{V}_{E^{2q}}. \tag{B.10}$$

This means that the vectors spanning the plane where the new reduced coordinates live (columns of $\mathbf{V}_0$) define an alternative coordinate chart of the same manifold, as long as the matrix $\mathbf{P}$ is nonsingular. When we add forcing ($\epsilon \neq 0$), we need to solve

$$\begin{aligned} \mathbf{r}_1(\boldsymbol{\Omega}t) &= \mathbf{W}_0\mathbf{A}\mathbf{v}_1(\boldsymbol{\Omega}t) + \mathbf{W}_0\mathbf{f}_1(\mathbf{0}, \boldsymbol{\Omega}t; 0), \\ \mathbf{v}_1(\boldsymbol{\Omega}t) &= \left(\mathbf{I} - \mathbf{V}_0\mathbf{W}_0\right)\mathbf{A}\mathbf{v}_1(\boldsymbol{\Omega}t) \\ &\quad + \left(\mathbf{I} - \mathbf{V}_0\mathbf{W}_0\right)\mathbf{f}_1(\mathbf{0}, \boldsymbol{\Omega}t; 0). \end{aligned} \tag{B.11}$$

which takes into account additional non-modal contributions to the forcing in reduced coordinates, as explained in Cenedese et al. [23].

Appendix C. Supplementary data

Supplementary material related to this article can be found online at https://doi.org/10.1016/j.ijnonlinmec.2024.104753.

References

[1] P. Benner, S. Gugercin, K. Willcox, A survey of projection-based model reduction methods for parametric dynamical systems, SIAM Rev. 57 (4) (2015) 483–531.
[2] C.W. Rowley, S.T. Dawson, Model reduction for flow analysis and control, Annu. Rev. Fluid Mech. 49 (2017) 387–417.
[3] A. Ghadami, B.I. Epureanu, Data-driven prediction in dynamical systems: recent developments, Philos. Trans. R. Soc. Lond. Ser. A Math. Phys. Eng. Sci. 380 (2229) (2022) 20210213.
[4] S.L. Brunton, B.R. Noack, P. Koumoutsakos, Machine learning for fluid mechanics, Annu. Rev. Fluid Mech. 52 (2020) 477–508.

[5] K. Taira, S.L. Brunton, S.T. Dawson, C.W. Rowley, T. Colonius, B.J. McKeon, O.T. Schmidt, S. Gordeyev, V. Theofilis, L.S. Ukeiley, Modal analysis of fluid flows: An overview, AIAA J. 55 (12) (2017) 4013–4041.
[6] C. Touzé, A. Vizzaccaro, O. Thomas, Model order reduction methods for geometrically nonlinear structures: a review of nonlinear techniques, Nonlinear Dynam. 105 (2) (2021) 1141–1190.
[7] G. Haller, S. Ponsioen, Nonlinear normal modes and spectral submanifolds: Existence, uniqueness and use in model reduction, Nonlinear Dynam. 86 (2016).
[8] S. Shaw, C. Pierre, Normal modes for non-linear vibratory systems, J. Sound Vib. 164 (1) (1993) 85–124.
[9] S. Shaw, C. Pierre, Normal modes of vibration for non-linear continuous systems, J. Sound Vib. 169 (3) (1994) 319–347.
[10] S.W. Shaw, C. Pierre, E. Pesheck, Modal analysis-based reduced-order models for nonlinear structures: An invariant manifold approach, Shock Vib. Dig. 31 (1999) 3–16.
[11] Y. Mikhlin, K.V. Avramov, Nonlinear normal modes of vibrating mechanical systems: 10 years of progress, Appl. Mech. Rev. (2023) 1–57.
[12] X. Cabré, E. Fontich, R. de la Llave, The parameterization method for invariant manifolds I: manifolds associated to non-resonant subspaces, Indiana Univ. Math. J. (2003) 283–328.
[13] A. Haro, R. de la Llave, A parameterization method for the computation of invariant tori and their whiskers in quasi-periodic maps: rigorous results, J. Differential Equations 228 (2) (2006) 530–579.
[14] G. Haller, B. Kaszás, A. Liu, J. Axås, Nonlinear model reduction to fractional and mixed-mode spectral submanifolds, Chaos 33 (6) (2023).
[15] S. Jain, G. Haller, How to compute invariant manifolds and their reduced dynamics in high-dimensional finite element models, Nonlinear Dynam. 107 (2022) 1–34.
[16] S. Jain, M. Li, T. Thurnher, G. Haller, SSMTool: Computation of invariant manifolds in high-dimensional mechanics problems, 2023.
[17] S. Jain, P. Tiso, G. Haller, Exact nonlinear model reduction for a von Karman beam: Slow-fast decomposition and spectral submanifolds, J. Sound Vib. 423 (2017).
[18] S. Ponsioen, S. Jain, G. Haller, Model reduction to spectral submanifolds and forced-response calculation in high-dimensional mechanical systems, J. Sound Vib. 488 (2020) 115640.
[19] M. Li, G. Haller, Nonlinear analysis of forced mechanical systems with internal resonance using spectral submanifolds, part II: Bifurcation and quasi-periodic response, Nonlinear Dynam. 110 (2) (2022) 1045–1080.
[20] M. Li, S. Jain, G. Haller, Nonlinear analysis of forced mechanical systemswith internal resonance using spectral submanifolds, part I: Periodic response and forced response curve, Nonlinear Dynam. 110 (2) (2022) 1005–1043.
[21] M. Cenedese, J. Axås, B. Bäuerlein, K. Avila, G. Haller, Data-driven modeling and prediction of non-linearizable dynamics via spectral submanifolds, Nature Commun. 13 (1) (2022) 872.
[22] M. Cenedese, J. Axås, H. Yang, M. Eriten, G. Haller, Data-driven nonlinear model reduction to spectral submanifolds in mechanical systems, Philos. Trans. R. Soc. Lond. Ser. A Math. Phys. Eng. Sci. 380 (2021).
[23] M. Cenedese, S. Jain, J. Marconi, G. Haller, Data-assisted non-intrusive model reduction for forced nonlinear finite elements models, 2023, arXiv:2311.17865.
[24] J. Axås, M. Cenedese, G. Haller, Fast data-driven model reduction for nonlinear dynamical systems, Nonlinear Dynam. 111 (9) (2023) 7941–7957.
[25] B. Kaszás, M. Cenedese, G. Haller, Dynamics-based machine learning of transitions in couette flow, Phys. Rev. Fluids 7 (2022).
[26] P.T. Cardin, P.R. Da Silva, M.A. Teixeira, On singularly perturbed filippov systems, Eur. J. Appl. Math. 24 (6) (2013) 835–856.
[27] P.T. Cardin, J.R. de Moraes, P.R. da Silva, Persistence of periodic orbits with sliding or sewing by singular perturbation, J. Math. Anal. Appl. 423 (2) (2015) 1166–1182.
[28] D. Weiss, T. Küpper, H. Hosham, Invariant manifolds for nonsmooth systems, Phys. D 241 (22) (2012) 1895–1902.
[29] D. Weiss, T. Küpper, H. Hosham, Invariant manifolds for nonsmooth systems with sliding mode, Math. Comput. Simulation 110 (2015) 15–32.
[30] T. Küpper, Invariant cones for non-smooth dynamical systems, Math. Comput. Simulation 79 (4) (2008) 1396–1408.
[31] R. Szalai, Model reduction of non-densely defined piecewise-smooth systems in Banach spaces, J. Nonlinear Sci. 29 (2019).
[32] A.Y. Karoui, R. Leine, Model reduction of a periodically forced slow–fast continuous piecewise linear system, Nonlinear Dynam. 111 (2023) 1–20.
[33] A.F. Filippov, Differential Equations with Discontinuous Righthand Sides, in: Mathematics and its Applications (Soviet Series), vol. 18, Kluwer Academic Publishers Group, Dordrecht, 1988.
[34] N. Fenichel, J.K. Moser, Persistence and smoothness of invariant manifolds for flows, Indiana Univ. Math. J. 21 (3) (1971) 193–226.
[35] R. Leine, H. Nijmeijer, Dynamics and Bifurcations of Non-Smooth Mechanical Systems, Vol. 18, 2004.
[36] H. Dankowicz, F. Schilder, Recipes for Continuation, Society for Industrial and Applied Mathematics, Philadelphia, PA, 2013.
[37] Hassler Whitney, The self-intersections of a smooth n-manifold in 2n-space, Ann. of Math. 45 (2) (1944) 220–246.